Miner Deposita (2016) 51:873–902
DOI 10.1007/s00126-016-0639-y

ARTICLE

Fluid evolution in a volcanic-hosted epithermal carbonate–base metal–gold vein system: Alto de la Blenda, Farallón Negro, Argentina

M. Florencia Márquez-Zavalía[1,2] · **Christoph A. Heinrich**[3]

Received: 15 April 2015 / Accepted: 19 January 2016 / Published online: 1 March 2016

Abstract Alto de la Blenda is a ~6.6-Ma intermediate-sulphidation epithermal vein system in the Farallón Negro Volcanic Complex, which also hosts the 7.1-Ma porphyry–Cu–Au deposit of Bajo de la Alumbrera. The epithermal vein system is characterised by a large extent and continuity (2 km × 400 m open to depth × 6 m maximum width) and an average gold grade of ~8 g/t. The vein is best developed within an intrusion of a fine-grained equigranular monzonite, interpreted as the central conduit of a stratovolcano whose extrusive activity ended prior to porphyry–Cu–Au emplacement at Bajo de la Alumbrera, which is in turn cut by minor epithermal veins. The Alto de la Blenda vein consists predominantly of variably Mn-rich carbonates and quartz, with a few percent of pyrite, sphalerite, galena and other sulphide and sulphosalt minerals. Four phases of vein opening, hydrothermal mineralisation and repeated brecciation can be correlated between different vein segments. Stages 2 and 3 contain the greatest fraction of sulphide and gold. They are separated by the emplacement of a polymictic breccia containing clasts of quartz feldspar porphyry as well as basement rocks. Fluid inclusions in quartz related to stages 2 to 4 are liquid rich with 2–4 wt% NaCl(eq). They homogenise between 160 and 300 °C, with very consistent values within each assemblage. Vapour inclusions are practically absent in the epithermal vein. Quartz fragments in the polymictic breccia contain inclusions of intermediate to vapour-like density and similar low salinity (~3 wt% NaCl(eq)), besides rare brine inclusions containing halite. Laser ablation–inductively coupled plasma–mass spectrometry (LA–ICP–MS) analyses of epithermal inclusions indicate high concentrations of K, Fe, As, Sb, Cs, and Pb that significantly vary within and through subsequent vein stages. Careful consideration of detection limits for individual inclusions shows high gold concentrations of ~0.5 to 3 ppm dissolved in the ore fluid, which contains variably high sulphur concentrations in excess over Fe and other chalcophile metals. Compositional variations are interpreted to reflect cooling and contraction of lower-density magmatic fluids at depth, like those preserved in porphyry clasts that were mechanically transported up by the polymictic breccia. Ore mineral precipitation from the magmatic fluid occurred by further cooling and possibly minor mixing with surface-derived water, leading to sulphide saturation, de-sulphidation of the magmatic fluid and consequent gold precipitation. The absence of flash boiling and/or reduction by carbonaceous host rocks has led to relatively modest but constant gold grades in the carbonate–base metal–gold veins of Alto de la Blenda.

Keywords Epithermal · Gold · Farallón Negro Volcanic Complex · Alto de la Blenda · Fluid evolution · Ore mineralogy · LA–ICP–MS

Editorial handling: D. Craw and G. Beaudoin

✉ M. Florencia Márquez-Zavalía
mzavalia@mendoza-conicet.gov.ar

[1] IANIGLA, CCT Mendoza, CONICET, CC 330, 5500 Mendoza, Argentina

[2] Mineralogía y Petrología, FAD, Universidad Nacional de Cuyo, Centro Universitario, 5502 Mendoza, Argentina

[3] Institute of Geochemistry and Petrology, Department of Earth Sciences, ETH Zurich, Clausiusstr. 25, CH-8092 Zurich, Switzerland

Introduction

The Farallón Negro mining district (also known as Agua de Dionisio district; Peirano 1944; Angelelli 1984) comprises a cluster of Cu–Au ore deposits genetically linked to a Miocene

magmatic complex with high-K calc-alkaline to shoshonitic affinities, known as the Farallón Negro Volcanic Complex (FNVC; Viramonte et al. 1984; Márquez-Zavalía 1988; Jones 1994, 1996; Sasso and Clark 1998, 1999; Müller and Forrestal 1998, 2000). This complex hosts two intensively studied, world-class porphyry deposits: Bajo de la Alumbrera (González 1975; Godeas and Segal 1980; Guilbert 1995; Mendez 1997; Wall 1997; Angera 1999; Ulrich et al. 1999; Ulrich and Heinrich 2002; Proffett 2003; Brown 2004; Halter et al. 2004, 2005; Harris et al. 2003, 2005, 2006; Heinrich et al. 2005, 2011; von Quadt et al. 2011) and Agua Rica (Koukharsky and Mirré 1976; Navarro 1986; Roco and Koukharsky 1999; Landtwing et al. 2002; Rojas and Perelló 2004; Franchini et al. 2009, 2011, 2015). Several smaller Au-bearing porphyry prospects with extensive alteration include Agua Tapada (Suchomel 1983; Gimeno Torrente et al. 2011), El Durazno (Allison 1986), El Espanto, San Lucas and Filo Colorado (JICA 1978–81). Associated epithermal deposits, besides Farallón Negro–Alto de la Blenda, include Mina Capillitas which provides the famous rhodochrosite veins of Argentina (JICA 1978–81; Márquez-Zavalía 1988, 1999, 2006, 2008 ; Breitenmoser 1999; Hug 1999; Márquez-Zavalía and Craig 2004; Putz et al. 2009) and the low-sulphidation epithermal prospect of Cerro Atajo (JICA 1978–81; Angelelli 1984; Márquez-Zavalía and Galliski 2007). Most authors interpret the Farallón Negro Volcanic Complex as the remnant of a large andesitic stratovolcano (e.g., Quartino 1962; Llambías 1970, 1972; Sillitoe 1973; Ulrich et al. 2002; Proffett 2003; Halter et al. 2004 and references therein), although Harris et al. (2006) present an alternative interpretation emphasising a local graben structure.

The Farallón Negro–Alto de la Blenda vein system is the most productive epithermal Au–Ag mine in NW Argentina. It is operated by YMAD, a joint venture owned by the National University of Tucumán, the province of Catamarca and the National Government of Argentina. During 2012 and 2013, the mine produced 9000 kg of Ag and 700 kg of Au per year. Ore reserves reported in June 2014 totalled 2.4 Mt with grades of 137.92 g/t Ag and 7.74 g/t Au. The deposit has been described by many authors (e.g. Quartino 1962; Sister 1963, 1965; Llambías 1970, 1972; JICA 1986–89; Alderete 1999; Montenegro and Morales 2004; Marquez-Zavalía and Heinrich 2011; Martinez et al. 2011; Salado Paz et al. 2011), but little original research has been completed using modern methods.

The deposit contains a few percent of pyrite + Fe-poor sphalerite + tennantite as its main sulphide assemblage, together with abundant Mn-rich carbonates besides quartz as dominant gangue minerals. It can be therefore classified as an intermediate-sulphidation Au–Ag deposit (Hedenquist et al. 2000) or a carbonate–base metal–gold vein system (Corbett and Leach 1998). Such epithermal deposits are commonly associated with porphyry ore systems (Sillitoe 2010), and their formation is suspected to involve a significant proportion of magmatic-hydrothermal fluids (Heinrich et al. 2004; Sillitoe 2010; Richards 2011, 2013; Wilkinson 2013; Heinrich and Candela 2014).

The aim of the present paper is to explore the fluid process of epithermal gold mineralisation in a geologically well-known subvolcanic setting. We focus on the geology and mineral paragenesis of the Alto de la Blenda vein system, as a basis for reconstructing the evolution of the fluids responsible for multistage mineralisation, using microthermometry and microanalytical investigations of fluid inclusions. We show that the deposit is a product of waning magmatic-hydrothermal activity, following porphyry-style ore formation at Bajo de la Alumbrera, and was formed dominantly by metal-rich magmatic-hydrothermal fluids of liquid-like density but low salinity.

Geology of the Cu–Au-mineralised Farallón Negro Volcanic Complex

Farallón Negro is a small mining town situated in Hualfín district, Catamarca province, Argentina, at 27° 16′ 26″ S and 66° 40′ 04″ W and 2600 m asl. The Farallón Negro mine is located about 6 km to the west of the Bajo de La Alumbrera mine and 320 km southwest of the city of San Miguel de Tucumán, in an isolated andesitic centre, the Farallón Negro Volcanic Complex (FNVC; Fig. 1). The ore district is located in the Sierras Pampeanas (Western Pampean Ranges), a tilt-block province controlling topography by Tertiary faulting of Palaeozoic and older basement rocks, reactivating NE-striking structural fabrics (Allmendinger 1986; Jordan and Allmendinger 1986; Fielding and Jordan 1988; McQueen and Beaumont 1989). Below the FNVC, the basement includes Cambrian metasediments intruded by the Ordovician Capillitas granite and other muscovite-bearing granitoids (Fig. 1; Ramos 1999).

On a plate-tectonic scale, the FNVC is located in the transition zone between two distinct tectonomagmatic segments of the Andes, an active volcanic segment (15° 24° S), where the Benioff zone is inclined about 30° to the east, and a segment that dips only 5° to 10° (27° 33° S), where Quaternary volcanism is lacking and Miocene magmatism is confined to isolated centres displaced towards the continent (González Bonorino 1950a, b; Barazangi and Isacks 1976; Sillitoe 1976; Isacks et al. 1982; Allmendinger et al. 1983; Jordan et al. 1983; Bevis and Isacks 1984; Jordan and Allmendinger 1986; Sasso and Clark 1998; Cahill and Isacks 1992; Coughlin et al. 1998; Kay et al. 1999; Landtwing et al. 2002). The FNVC is one of these centres in the distal part of the Miocene-Recent volcanic arc. It has also been grouped with the Carachipampa-Farallón Negro transverse volcanic chain of the Central Andes, which has

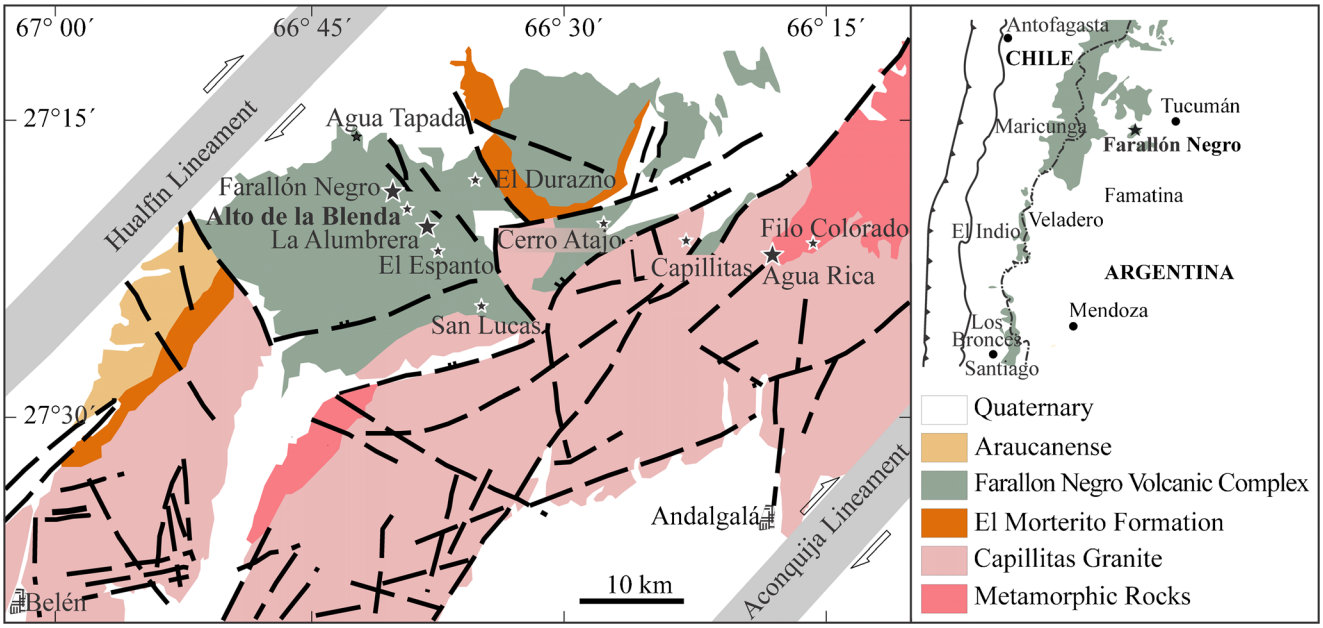

Fig. 1 Geological map of the FNVC area including lithological units, major structures, main mines and prospects (modified from Marquez-Zavalía 2008)

dominant shoshonitic affinities (Viramonte et al. 1984). The FNVC is confined between two NE trending structures, the Hualfín and Aconquija lineaments (Mon 1976; Ramos 1977). Associated NW-striking faults, developed as tensional fractures, control the emplacement of some of the deposits and prospects, and the largest deposits are aligned in an E–W direction (Fig. 1).

Magmatic rocks of the FNVC were emplaced in a block-faulted, tectonically depressed area of the crystalline basement, and detailed mapping by Llambías (1972) indicates that the centre of a long-lived stratovolcano was located near the Alto de la Blenda monzonite stock (Fig. 1). The most abundant rocks of the FNVC represented in the study area of Fig. 2 are andesite and basaltic andesite emplaced as lavas and volcanic breccias, defining a locally mappable stratigraphy (Llambías 1970, 1972; Halter et al. 2004). These extrusive rocks are intermittently intruded by subvolcanic stocks, including the La Chilca andesite porphyry as one of the oldest (9.0 ± 0.2 Ma, ^{40}Ar–^{39}Ar, Sasso 1997 in Halter et al. 2004) and the Alto de la Blenda monzonite as one of the younger intrusions (7.6 ± 0.3 Ma, ^{40}Ar–^{39}Ar, Sasso 1997 in Halter et al. 2004), demonstrating long-lived volcanic activity predating hydrothermal ore formation. The monzonite is the largest intrusion (6 km^2 of exposure) and differs from others by having an equigranular texture, composed mainly by plagioclase, K-feldspar, quartz and pyroxene with minor biotite and amphibole. This stock is surrounded by a swarm of radially oriented dykes with monzonitic composition, showing preferential alignment in a NE–SW direction that is coincident with the elongation of the La Chilca andesite porphyry (Llambías 1970, 1972) and with many other magmatic and hydrothermal vein structures (Fig. 2). This common orientation reflects a preferred NW–SE direction of fracture opening, nearly parallel to the major lineaments localising the FNVC on a larger scale (Fig. 1). Field evidence for thrust faulting on some of the NW–SE faults at the time of magmatism (Llambías 1970, 1972; Halter et al. 2004; Hug 1999; Breitenmoser 1999) indicates pull-apart opening of dykes and veins in a right-lateral and transpressional stress environment.

Hydrothermal ore deposits of different styles formed during the final stages of magmatism and can be temporally bracketed by intersection relationships, igneous intrusion contacts and radiometric dating. Porphyry–Cu–Au–Mo ore formation at Bajo de la Alumbrera, located approximately 5 km SE of the Alto de la Blenda monzonite stock, postdated all extrusive activity by ~0.3 Ma (Halter et al. 2004) and involved several pulses of veining bracketed within a short time interval of 7.216 ± 0.018 to 7.164 ± 0.057 Ma by vein/intrusion intersections and U-Pb zircon ages (von Quadt et al. 2011). All dacite porphyries and Cu–Au-mineralised stockwork veins at Bajo de la Alumbrera were cut by steep normal faults filled with subeconomic gold-mineralised base-metal carbonate veins (Proffett 2003; Meier 2008; Meier et al. 2008). These late fractures show NW–SE orientation and mineralogical characteristics similar to the much wider epithermal veins mined at Farallón Negro–Alto de la Blenda and probably represent a continuous vein system. Near the other extremity of this vein swarm, small carbonate–base metal–gold veins were historically mined at Macho Muerto (Fig. 2), hosted by andesitic volcanic rocks close to the Macho Muerto quartz–plagioclase porphyry intrusion. In

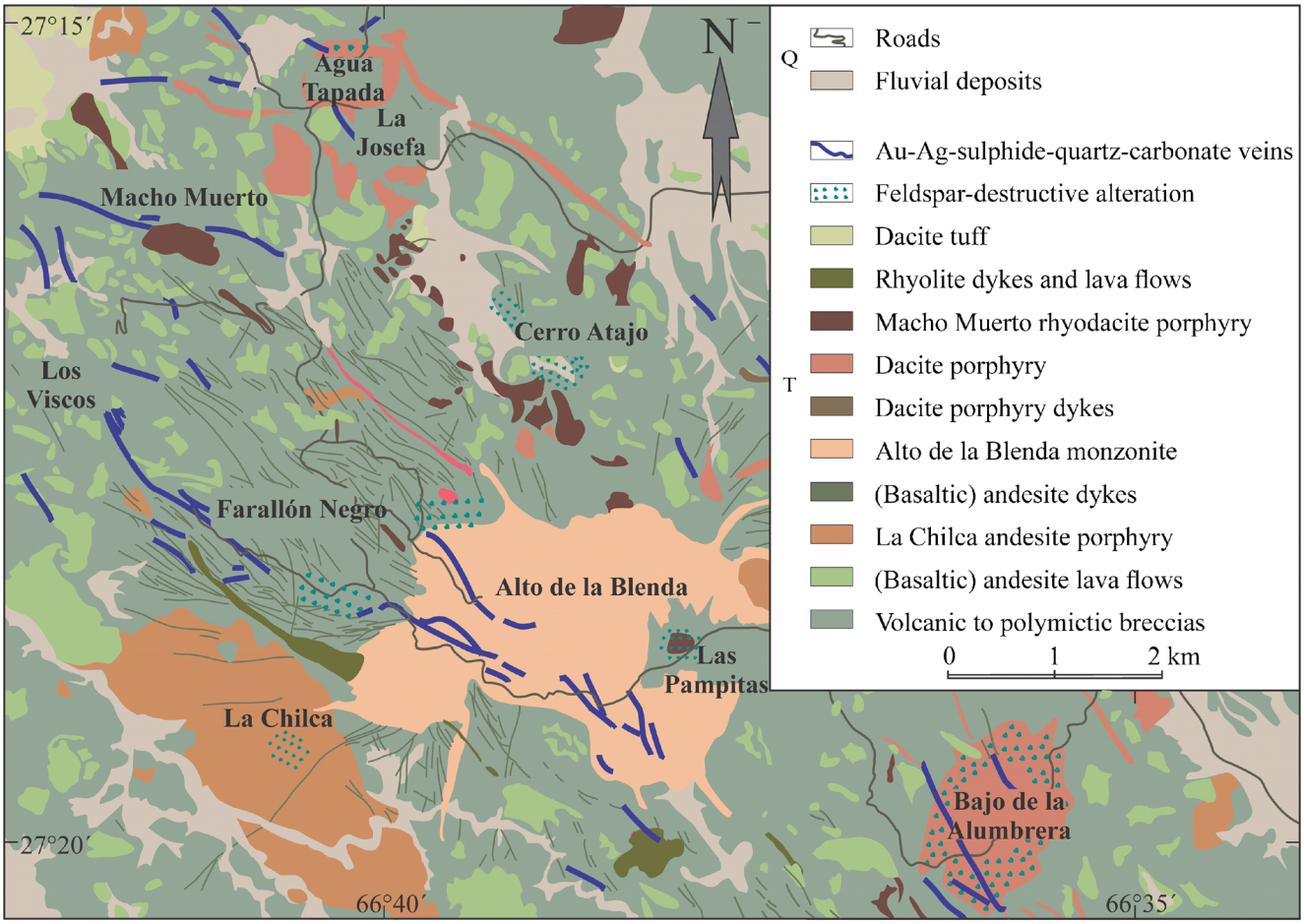

Fig. 2 Geological map of the central part of the FNVC, modified from JICA (1986–89, largely based on Llambías 1970, YMAD exploration maps, and mine geology of Bajo de la Alumbrera by Proffett 2003)

contrast to dacite porphyries at Bajo de la Alumbrera and Agua Tapada, the rhyodacite porphyry of Macho Muerto is completely unaltered with a flow-banded, formerly glassy, matrix and contains fresh plagioclase and sanidine which was dated initially at 6 ± 1 Ma by Linares and González (1990) and more recently at 6.26 ± 0.15 Ma (^{40}Ar–^{39}Ar, Halter et al. 2004) and 6.04 ± 0.07 Ma (^{40}Ar–^{39}Ar, Sasso 1997, in Halter et al. 2004). Detailed field observations confirmed the absence of any carbonate veins within the Macho Muerto stock, whereas numerous veins crosscut the andesites in its vicinity, indicating that the Macho Muerto stock was emplaced after the epithermal veins. These observations bracket the formation of the epithermal veins between 7.164 ± 0.057 and 6.26 ± 0.15 Ma. This age bracket is consistent with a whole-rock Ar–Ar age on quartz–sericite alteration associated with the Alto de la Blenda gold vein of 6.55 ± 0.14 Ma (Sasso and Clark 1998). Due to the lack of adularia (not found in any of the samples investigated), these brackets currently provide the best estimate of the age of the epithermal gold mineralisation. The hypogene Au–Ag–base metal sulphide veins were partly oxidised to a supergene Mn oxide-rich assemblage, which was dated by K–Ar analysis of cryptomelane at ca. 2.7 ± 0.8 Ma (McBride 1972, recalculated by Sasso and Clark 1998). Sasso (1997) suggested that the ~3-Ma interval between hypogene mineralisation at ~6.6 Ma and supergene oxidation at ~2.7 is a plausible measure for the main period of erosion of the former stratovolcano to the present land surface.

The Farallón Negro–Alto de la Blenda epithermal vein system

Epithermal veins of greatest width and best continuity occur within and NE of the Alto de la Blenda monzonite stock. Two major but partly connected vein sets were mined, the original Farallón Negro vein and the currently producing Alto de la Blenda vein (Montenegro and Morales 2004). The latter is divided, mainly for mining purposes, into the Laboreo, Esperanza and Esperanza SE vein segments. The Alto de la Blenda vein is the focus of this research (Fig. 3). The main segments of this vein are hosted by andesite (NW part of Laboreo segment) and the

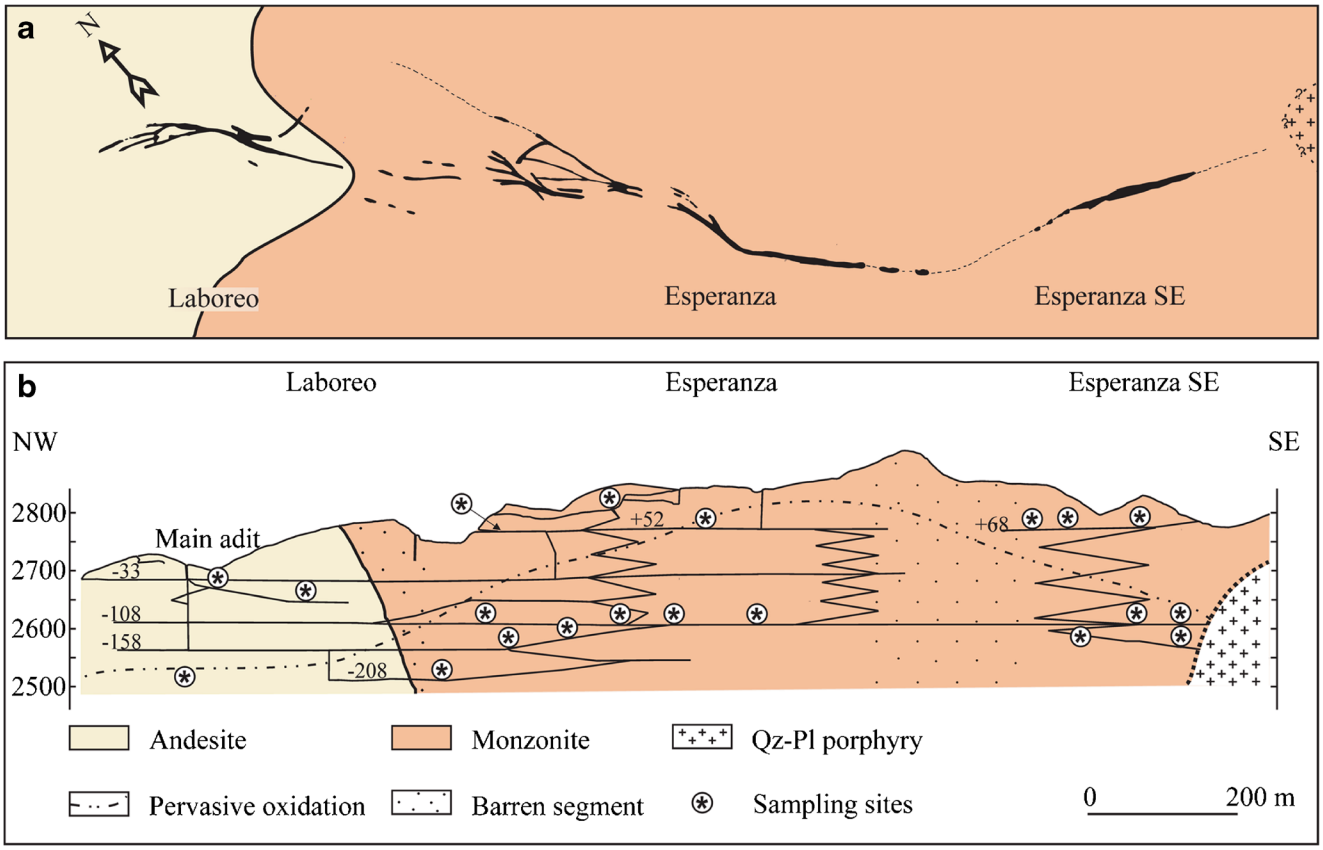

Fig. 3 **a** Plan projection of the Alto de la Blenda vein, showing the Laboreo, Esperanza and Esperanza SE segments (*black*) and linking thin zones of shearing and alteration with no or subeconomic mineralisation (*dashed lines* in **a**, stippled areas in **b**). **b** Vertical long section projecting the steeply NE-dipping Alto de la Blenda vein, with lithologies, names of mined vein segments, approximate depth extent of locally pervasive oxidation, access tunnels and sampling sites

Alto de la Blenda monzonite (rest of Laboreo, Esperanza and Esperanza SE segments). Subeconomic extensions of the veins cut a recently discovered quartz–plagioclase porphyry north of the southeastern end of the Esperanza SE segment, which does not crop out at surface. The vein set roughly follows a NW–SE orientation with numerous irregularities, branches and anastomosing subdivisions, and it has an average dip of 80° to 60° towards the NE. The Laboreo segment is 1500 m long and 2 m wide on average, the Esperanza segment is 1100 m long and 6 m wide and the Esperanza SE segment is about 400 m long and 4 m wide. The maximum vertical exposure is 300 m, and the limited information from drilling data shows that the system is open to greater depth. The economically mineralised segments (>2 m) are separated by highly altered shear zones that host thin veins or are completely barren. No systematic structural study and kinematic analysis of this system was performed, but from our observations on the geometry of the veins, dip-slip normal faulting is suspected. It would explain, among other characteristics of the deposit, the more gently inclined barren fault gap between Esperanza and Esperanza SE segments (Fig. 3).

The veins have generally sharp contacts and show macroscopic evidence of multiple events of forceful brittle opening and brecciation, alternating with hydrothermal mineral precipitation into formerly open space (Fig. 4). All along the vein, at least four stages of hydrothermal quartz–carbonate–sulphide mineralisation can be recognised, separated by events of re-fracturing and intense brecciation (Fig. 4a–c). Sulphide–carbonate–quartz crusts overgrowing earlier fragments and fracture surfaces are ubiquitous, but open cavities are rare and invariably lined by euhedral quartz, but never contain free-standing crystals of ore minerals. Even though the large veins commonly have a banded appearance parallel to the contacts, we have observed no vein section indicating a simple inward crystallisation of successive layers, but instead found ubiquitous evidence of re-opening and brecciation.

A zone of polymictic breccia is exposed along the hanging wall of the Alto de la Blenda vein. Although not fully mapped, it occurs in all segments of the vein and is best developed in the central Esperanza segment (Fig. 4a) where it can reach a thickness of several metres. The breccia has a mostly sandy matrix altered to clay minerals, supporting abundant partly rounded clasts of andesite and monzonite up to 10 cm in size

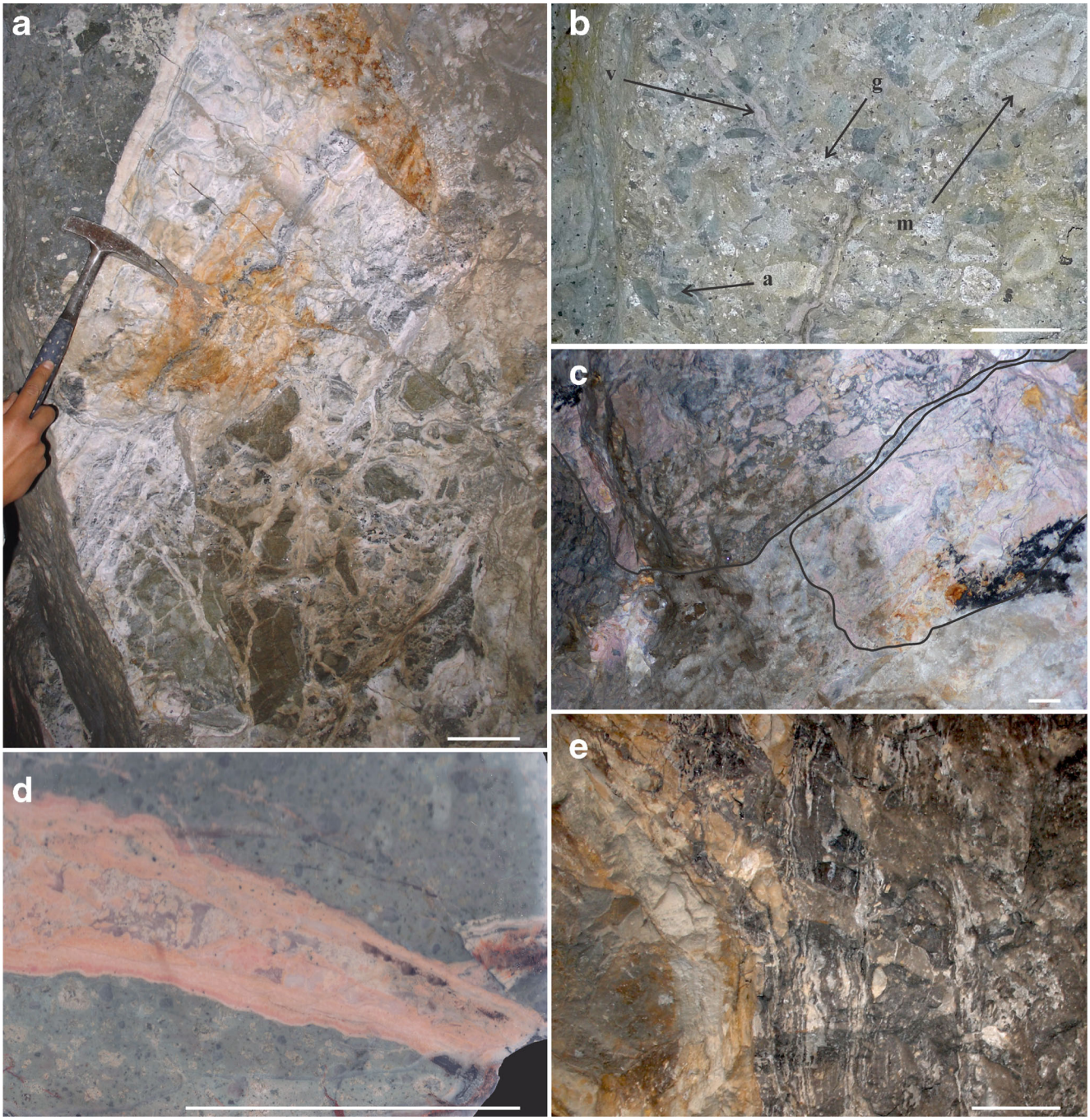

Fig. 4 Outcrop-scale geological relations at Alto de la Blenda vein (scale bar is 10 cm in all pictures). **a** NE contact of the Esperanza segment, showing multistage hydrothermal vein with clasts of chlorite-sericite-altered monzonite, cutting polymictic breccia of the hanging wall (*left of hammer*). **b** Hanging-wall breccia, with locally flow-banded sandy cement (*left edge of photo*), containing clasts of monzonite (*m*) commonly concentrically altered, andesite (*a*) and rare clasts of basement granite (*g*); the breccia is cut by an irregular pink carbonate veinlet (*v*). **c** Interior part of the Esperanza segment showing at least three stages of hydrothermal quartz–carbonate–sulphide mineralisation separated by two events of intense brecciation (second-stage large clasts emphasised by *thin lines*). **d** Quartz–plagioclase porphyry intrudes the Alto de la Blenda monzonite north of the Esperanza SE segment before being cut by carbonate–base metal vein. **e** Vertical contact of completely oxidised Esperanza segment close to upper adit, showing well-preserved banding of original hydrothermal quartz (*white*) and Mn oxides (*black*); note thin halo of sericite–pyrite alteration (*white yellow*) grading into chlorite-altered monzonite (*grey*)

(Fig. 4b). It also contains smaller fragments of muscovite-bearing basement granite and of quartz–plagioclase porphyry resembling the small intrusion at the southeastern end of the Esperanza SE segment (Fig. 3b). Moreover, angular clasts of earlier hydrothermal vein material with quartz–pyrite–sphalerite–minor galena and chalcopyrite (Fig. 4b) can be found. Contacts of the breccia are generally sharp, to the monzonite in the hanging wall and to the Alto de la Blenda vein in the footwall, but the latter is complex due to fragments of earlier veins included in it and later veins cutting the breccia after its lithification.

Thin vein haloes in monzonite (few cm) and more extensive alteration in volcanic host rocks, breccias and porphyries are dominated by sericite–chlorite–clay minerals (smectite, JICA 1986–89).

Supergene oxidation variably overprints the hydrothermal vein minerals along a sharp reaction front (Fig. 4e). Leaching of all sulphides and conversion of Mn carbonates to Mn oxides and hydroxides are pervasive in all surface outcrops of the veins and gave the Farallón Negro vein its name: the 'Black Wall'. This replacement seems volume conserving, leaving only quartz intact with its original banding and local open vugs. Pervasive supergene oxidation locally extends to the deepest levels of the active mine, but most of the presently mined ore is completely unoxidised.

Sampling and analytical methods

Fieldwork at the Farallón Negro mine was conducted during several visits between 2004 and 2013. Samples were obtained from all vein segments of Alto de la Blenda including underground workings, drill cores and outcrops. Underground samples of ore and gangue minerals were selected where time relations between multiple mineralisation stages could be mapped at the scale of rock faces. Sample locations and descriptions of different units were referenced to mine maps and

Table 1 Representative chemical analyses of sulphides from Alto de la Blenda

Mineral	Py	Sp2 (c)	Sp2 (b)	Ccp	Gn	Hes	Crv	Jlp	Mk	Cmk	Pzh
S wt.%	50.72	32.86	32.43	34.39	13.55	0.00	5.16	14.41	14.54	17.52	12.05
Mn	0.00	0.00	0.00	0.00	0.04	0.00	0.00	0.00	0.00	0.00	0.00
Fe	45.81	0.12	1.12	30.64	0.00	0.00	0.00	0.32	0.00	0.00	0.00
Cu	0.32	0.12	0.96	34.59	0.03	0.00	1.87	14.52	23.71	54.03	4.31
Zn	0.85	67.02	65.55	0.22	0.03	0.08	0.48	0.29	0.43	0.14	0.00
As	0.21	n.a.	n.a.	0.00	0.00	0.00	0.00	0.00	0.00	0.00	0.00
Ag	0.29	0.00	0.00	0.00	0.10	61.62	69.60	69.62	60.48	27.78	51.13
Cd	0.01	0.15	0.09	0.00	0.05	0.00	0.00	0.00	0.52	0.00	0.00
In	0.00	0.10	0.13	0.00	0.00	0.00	0.00	0.00	0.00	0.00	0.00
Te	0.00	0.00	0.00	0.00	0.02	37.51	23.41	0.00	0.00	0.00	0.00
Au	0.19	0.00	0.00	0.00	0.00	0.00	0.00	0.70	0.00	0.00	33.22
Pb	0.00	0.00	0.00	0.00	86.31	0.00	0.00	0.00	0.00	0.00	0.00
Total	98.39	100.38	100.27	99.84	100.13	99.21	100.52	99.86	99.68	99.48	100.71
S apfu	1.956	0.997	0.986	1.978	1.003	0.000	0.941	2.017	0.972	0.990	3.114
Mn	0.000	0.000	0.000	0.000	0.002	0.000	0.000	0.000	0.000	0.000	0.000
Fe	1.014	0.002	0.020	1.012	0.000	0.000	0.000	0.026	0.000	0.000	0.000
Cu	0.006	0.002	0.015	1.004	0.001	0.000	0.172	1.025	0.801	1.540	0.562
Zn	0.016	0.997	0.978	0.006	0.001	0.004	0.043	0.020	0.014	0.004	0.000
As	0.003	0.000	0.000	0.000	0.000	0.000	0.000	0.000	0.000	0.000	0.000
Ag	0.003	0.000	0.000	0.000	0.002	1.978	3.775	2.896	1.203	0.466	3.927
Cd	0.000	0.001	0.001	0.000	0.001	0.000	0.000	0.000	0.010	0.000	0.000
In	0.000	0.001	0.001	0.000	0.000	0.000	0.000	0.000	0.000	0.000	0.000
Te	0.000	0.000	0.000	0.000	0.000	1.018	1.073	0.000	0.000	0.000	0.000
Au	0.001	0.000	0.000	0.000	0.000	0.000	0.000	0.016	0.000	0.000	1.397
Pb	0.000	0.000	0.000	0.000	0.989	0.000	0.000	0.000	0.000	0.000	0.000
Total	3.000	2.000	2.000	4.000	2.000	3.000	6.000	6.000	3.000	3.000	9.000

Py pyrite, *Sp2* sphalerite from stage 2, *Ccp* chalcopyrite, *Gn* galena, *Hes* hessite, *Crv* cervelleite, *Jlp* jalpaite, *Mk* mckinstryite, *Cmk* Cu-rich mckinstryite, *Pzh* penzhinite, *(c)* core, *(b)* border

Table 2 Representative chemical analyses of sulphosalts from Alto de la Blenda

Mineral	Ttr	Tnt	Prc	Plb	Cprc	Cplb
S wt.%	23.99	27.82	16.50	15.49	16.88	16.84
Mn	0.60	0.58	0.00	0.00	0.00	0.00
Fe	0.69	1.83	0.00	0.00	0.00	0.01
Cu	36.57	38.83	7.31	6.32	13.02	14.73
Zn	7.09	6.62	0.00	0.00	0.15	0.00
As	3.45	17.75	5.27	2.43	4.97	3.07
Ag	1.46	3.31	67.63	66.97	61.14	58.89
Sb	25.28	3.20	2.30	6.47	3.63	6.56
Te	0.00	0.03	0.00	1.36	0.00	0.00
Au	0.00	0.01	0.00	0.00	0.00	0.00
Total	99.13	99.99	99.01	99.05	99.79	100.10
S apfu	12.595	12.848	11.041	10.778	10.968	10.894
Mn	0.185	0.157	0.000	0.000	0.00	0.000
Fe	0.208	0.486	0.125	0.000	0.00	0.002
Cu	9.688	9.047	2.468	2.220	4.269	4.809
Zn	1.825	1.498	0.000	0.000	0.047	0.000
As	0.775	3.508	1.509	0.723	1.382	0.849
Ag	0.228	0.454	13.452	13.854	11.712	11.327
Sb	3.495	0.389	0.405	1.187	0.621	1.118
Te	0.000	0.371	0.000	0.238	0.00	0.000
Au	0.000	0.241	0.000	0.000	0.00	0.000
Total	29.000	29.000	29.000	29.000	29.00	29.000

Trt tetrahedrite, *Tnt* tennantite, *Prc* pearceite, *Plb* polybasite, *Cprc* cupropearceite, *Cplb* cupropolybasite

sections (Fig. 3). Large slabs were sampled where possible, and conventional thin, polished and double-polished sections were studied under the polarising microscope.

Chemical analyses of gold, sulphides, sulphosalts and tellurides were performed with a Cameca SX-100 electron microprobe (EMP) at the Department of Geological Sciences, University of Manitoba, Winnipeg, Canada, and with a Jeol JXA-8200 Superprobe at the Department of Earth Sciences, ETH Zürich, Switzerland, with a beam diameter of 1 to 5 μm and an acceleration potential of 15 kV. A sample current of 20 nA measured on a Faraday cup and a counting time of 20 s for the elements and 10 s for the background was used. The standards and analytical lines selected were as follows: S, Fe, Cu ($CuFeS_2$, $K\alpha$), Mn ($Mn^{2+}S$, $K\alpha$), Zn (ZnS, $K\alpha$), Ga, As (GaAs, $L\alpha$), Ge (Ge, $L\alpha$), Se (Bi_2Se_3, $L\beta$), Ag (Ag_2Se, $L\alpha$), Cd (CdSe, $L\alpha$), In (InAs, $L\alpha$), Sn (SnO_2, $L\beta$), Sb (Sb_2S_3, $L\alpha$), Te (PbTe, $L\alpha$), W ($CaWO_4$, $M\alpha$), Au ($Au_{80}Ag_{20}$, $M\alpha$), Tl ($TlAsS_2$, $L\alpha$), Pb (PbS, $M\alpha$) and Bi (Bi_2Se_3, Mα). All samples were carefully checked before analyses, under the highest magnification, to avoid analysing small inclusions that could be present in the analysed phase, and analysis spots were selected in homogeneous, inclusion-free areas. The Canadian and Swiss data were reduced using the PAP routine by Pouchou and Pichoir (1985) and the CITZAF routine (Armstrong 1993), respectively. All elements listed above were tested in all phases, but many were below the typical detection limit of ~0.01 wt% (Tables 1 and 2).

Fluid inclusion studies were performed at ETH-Zürich, using a Linkam THSMG-600 heating-freezing stage combined with a Nikon Eclipse 6500 Pol microscope and a Nikon Digital Eclipse DXM-1200 camera. Calibration procedure used synthetic fluid inclusion standards (SYN FLINC): CO_2 melting point (−56.6 °C), H_2O melting point (0.0 °C) with a ±0.2 °C precision, and pure H_2O critical homogenisation (374.1 ± 3 °C). All microthermometrical studies (Table 3) were performed on fluid inclusion assemblages (FIAs) previously defined by petrography, following Goldstein and Reynolds (1994) criteria. The apparent salinities of the Alto de la Blenda fluid inclusions are reported in wt% NaCl(eq), based on the final ice melting temperature (Bodnar and Vityk 1994). No clathrates were observed, and the clear laser ablation-inductively coupled plasma-mass spectrometry (LA–ICP–MS) signals of all inclusions indicate that salt rather than dissolved CO_2 is dominantly responsible for freezing point depression (cf. Hedenquist and Henley 1985).

LA–ICP–MS studies were performed with a Perkin Elmer Elan 6100 ICP-MS instrument combined with the Lambda Physik 193-nm ArF excimer laser system prototype developed at ETH-Zürich (Günther et al. 1998; Heinrich et al. 2003; Pettke et al. 2004), with an energy density of up to 25 J/cm^2 and a pulse frequency of 10 Hz. $A \approx 1$ cm^3 internal volume ablation cell allowed fast aerosol transport with an He–Ar carrier gas from the sample to the ICP. To maximise detection in these small low-salinity inclusions, a restricted element menu with Si, Na, S, K, Fe, Cu, As, Ag, Sb, Cs, Au and Pb was used, with extended 70 ms dwell times for Au, 20 ms for S, As, Ag and Sb and 10 ms for the remaining elements. The SILLS software (Guillong et al. 2008) was used to reduce the data and calculate element concentrations, using an empirical correction for K as the second-most important salt component (Günther et al. 1998; Heinrich et al. 2003). Limits of detection (LOD) for S are relatively high, and careful host and background corrections were performed for each fluid inclusion signal, after the ablation chamber was repeatedly cleaned to minimise contamination (Guillong et al. 2008; Seo et al. 2011). For sphalerite-hosted fluid inclusions, Zn, S, Fe and Cu could not be analysed.

Recent microanalytical studies have explored the challenges of estimating elemental detection limits (maximum possible concentrations) in a palaeo-fluid based on multiple single-inclusion analyses, and of quantifying average concentrations of an element which is detected only in some of the inclusions within a fluid inclusion assemblage

Table 3 Average microthermometry data of fluid inclusions in quartz and sphalerite from Alto de la Blenda

Mineral	Vein segment	Sample #	FIA type	Salinity wt% NaClequiv.					Th (°C)				
				Max	Min	Avg.	SD	*n*	Max	Min	Avg.	SD	*n*
Qp	ESE	301-1a-FIA1	P	2.9	2.2	2.5	0.2	6					
Qp	ESE	301-1a-FIA2	P	2.4	1.9	2.2	0.2	5					
Qp	ESE	301-1a-FIA3	P	2.6	1.9	2.2	0.3	5					
Qp	ESE	301-1a-FIA4	P	35.3	34.5	34.8	0.4	4					
Q1	L	122.a-Ch.2-FIA1	P	2.2	2.1	2.2	0.1	6	212.0	203.5	206.5	3.6	5
Q1	L	122.a-Ch.2-FIA2	P	2.9	2.2	2.5	0.2	5	218.7	211.6	216.1	2.8	5
Q1	L	122.a-Ch.2-FIA3	P			2.6	0.0	1					
Q1	L	122.a-Ch.5-A1-FIA1a	PS	3.4	2.4	2.7	0.4	5	207.8	193.1	201.2	5.3	5
Q1	L	122.a-Ch.5-A1-FIA1b	PS	2.9	2.6	2.7	0.1	6	212.9	208.0	210.2	1.7	5
Q1	L	122.a-Ch.5-A1-FIA2	PS	3.4	3.1	3.2	0.2	7	205.6	190.4	197.5	6.8	5
Q1	L	122.a-Ch.5-A2-FIA1	P	2.6	2.1	2.4	0.2	4	214.4	203.2	207.6	6.0	3
Q1	L	122.a-Ch.5-A2-FIA2	P	2.6	2.4	2.5	0.1	7	215.3	201.1	206.7	4.5	8
Q1	E	105-Chip 2-FIA3	P	3.4	3.1	3.2	0.1	6	261.9	257.9	259.7	1.4	6
Q1	E	204.2-Ch.1.a-FIA1	P	2.4	2.4	2.4	0.0	4	198.2	194.2	196.2	2.8	2
Q1	E	204.2-Ch.1.a-FIA2	PS	2.4	2.2	2.3	0.1	8	183.2	171.4	175.4	5.6	5
Q1	E	204.2-Ch.1.a-FIA3	PS	4.3	2.1	3.2	1.3	4	207.2	193.4	200.3	9.8	2
Q2a	L	001(G)-FIA1	P						265.1	263.7	264.6	0.5	8
Q2a	L	001(G)-FIA2	P	3.1	2.4	2.7	0.2	7	265.2	263.9	264.5	0.5	7
Q2a	L	001(R)-FIA2	PS	2.6	2.2	2.3	0.1	8	209.9	208.5	209.1	0.4	9
Q2a	L	122.a-Ch.5-A1-FIA3	P	2.9	2.7	2.9	0.1	7	212.4	192.3	204.5	8.5	6
Q2a	E	101.b-Ch.1a-FIA1	P	3.9	3.4	3.6	0.2	8	249.2	245.4	247.3	2.7	6
Q2a	E	003-A.7-FIA1	P	4.7	3.4	4.0	0.4	7	238.7	230.9	233.5	2.8	7
Q2a	E	003-A.7-FIA4	P	4.3	3.4	3.8	0.4	5	295.7	290.8	292.9	2.5	3
Q2a	E	003-A.7-FIA5	P	4.5	4.2	4.4	0.2	6	174.9	167.9	172.3	2.5	6
Q2a	E	002.4-FIA1	PS	4.3	4.2	4.3	0.1	4	220.5	207.0	212.0	5.9	4
Q2a	E	002.4-FIA2	PS	4.8	3.2	4.1	0.7	7	215.1	197.3	206.5	6.4	5
Q2a	E	105-Ch.2-FIA1	P	3.6	3.6	3.6	0.0	3	190.9	190.2	190.5	0.4	3
Q2a	E	105-Ch.2-FIA4	P	3.7	3.2	3.6	0.3	3	184.8	179.9	182.0	2.5	3
Q2b	L	122.b-Ch.2-FIA1	PS	3.1	2.7	2.9	0.2	6	216.6	208.7	214.1	3.3	6
Q2b	L	122.b-Ch.2-FIA2	P	3.2	2.9	3.1	0.1	8	200.4	195.4	198.1	2.0	7
Q2b	L	122.b-Ch.2-FIA3	P	2.2	2.1	2.1	0.1	5	209.5	203.4	207.8	3.0	4
Q2b	L	122.b-Ch.2-FIA4	P	2.9	2.7	2.8	0.1	6	212.3	198.7	207.9	5.6	6
Q2b	L	122.b-Ch.2-FIA5	P	3.1	2.9	3.0	0.1	6	233.5	220.5	225.7	4.7	5
Q2b	E	003-A.8-FIA2	PS	4.0	3.4	3.6	0.3	4	265.7	256.1	260.2	3.6	6
Q2b	E	003-A.8-FIA3	P	2.9	2.6	2.8	0.2	3	211.7	210.3	211.0	1.0	2
Q2b	E	003-A.8-FIA5	P	4.7	3.7	4.2	0.4	7	225.6	212.2	220.7	5.9	5
Q2b	E	105-Ch.1-FIA1	P	4.2	3.4	3.8	0.3	5	256.2	254.2	255.5	0.8	5
Q2b	E	105-Ch.1-FIA2	P	4.2	3.9	4.0	0.2	5	204.1	193.7	197.3	5.9	5
Q2b	ESE	132-Ch.2-FIA1	P	2.6	2.2	2.4	0.1	6	207.9	203.9	205.9	2.8	2
Q2b	ESE	132-Ch.2-FIA2	PS	2.4	2.2	2.3	0.1	3	209.3	196.7	203.0	8.9	2
Q2b	ESE	132-Ch.2-FIA3	P	2.2	2.1	2.1	0.1	7	212.3	204.1	207.2	4.5	3
Q2b	ESE	132-Ch.2-FIA4	P	3.1	2.2	2.6	0.3	8	220.3	207.0	213.6	5.9	7
Q2	BLA	BLA 200.280-6	PS						285.6	273.8	279.6	6.5	4
Q2	BLA	BLA 200.280-7	PS	3.2	2.7	2.9	0.2	4	285.5	271.9	275.6	5.6	5

Table 3 (continued)

Mineral	Vein segment	Sample #	FIA type	Salinity wt% NaClequiv.					Th (°C)				
				Max	Min	Avg.	SD	*n*	Max	Min	Avg.	SD	*n*
Q2	BLA	BLA 200.280-8	PS						297.1	292.7	294.9	3.1	2
Q2	BLA	BLA 200.280-9	PS	2.6	2.2	2.4	0.1	4	298.4	286.7	292.3	5.9	3
Sp2	E	35-Ha-FIA1	P	1.9	1.2	1.4	0.3	7	264.9	258.1	262.2	3.0	7
Sp2	E	35-Ha-FIA2	P	2.6	2.2	2.4	0.2	3	225.2	219.9	223.3	3.0	3
Sp2	E	35-Hb-FIA1	PS	2.1	1.9	2.0	0.1	4	222.4	219.8	221.0	1.1	4
Sp2	E	35-Hb-FIA2	P	2.2	1.9	2.1	0.1	4	215.4	211.3	213.5	1.7	4
Sp2	E	35-Hb-FIA3	P	2.2	1.9	2.1	0.1	7	213.9	207.1	211.8	2.3	7
Sp2	BLA	BLA 200.280-1	P	2.7	2.2	2.5	0.2	5	253.3	245.7	248.8	3.0	5
Sp2	BLA	BLA 200.280-2	P			2.7	0.0	1	279.5	277.9	278.9	0.9	3
Sp2	BLA	BLA 200.280-3	PS	3.9	3.7	3.8	0.1	3	253.3	245.7	248.8	3.0	5
Sp2	BLA	BLA 200.280-4	P						269.3	266.3	267.6	1.3	5
Q3a	L	024-B1-FIA1	P	3.4	3.2	3.3	0.1	6	189.3	178.0	182.9	4.2	6
Q3a	L	024-B1-FIA2	P	5.1	4.8	5.0	0.2	3	185.0	180.4	182.8	2.3	4
Q3a	L	024-B1-FIA4	P	3.6	3.2	3.4	0.2	4	206.8	205.9	206.4	0.6	2
Q3a	L	024-B1-FIA5	P	4.5	3.9	4.0	0.2	7	211.9	193.7	202.4	6.5	7
Q3a	E	103.b-FIA1	PS	4.8	4.5	4.7	0.1	5					
Q3a	E	127-Ch.5-FIA1	P	1.9	1.6	1.7	0.2	6	218.2	208.3	211.7	3.4	7
Q3a	E	127-Ch.5-FIA2	PS	2.9	1.2	2.3	0.6	6	213.1	196.8	205.3	5.8	8
Q3a	E	127-Ch.5-FIA3	PS	1.6	1.4	1.4	0.1	6	213.2	199.9	205.5	6.1	5
Q3a	E	127-Ch.5-FIA5	P	1.6	1.6	1.6	0.0	6	187.5	177.2	182.5	4.2	4
Q3a	E	127-Ch.5-FIA6	P	1.4	1.4	1.4	0.0	6	208.9	200.1	204.2	4.4	4
Q3a	E	127-Ch.5-FIA7	P	3.4	1.4	2.7	1.0	6	214.6	206.7	211.6	3.7	4
Q3a	ESE	110-Ch.1-FIA1	P	2.4	1.7	2.1	0.3	5	223.4	221.2	222.7	1.3	3
Q3a	ESE	110-Ch.1-FIA3	P	2.2	2.1	2.2	0.1	5	221.7	221.5	221.6	0.1	5
Q3a	ESE	110-Ch.1-FIA4	PS	4.0	3.9	3.9	0.1	5	245.0	234.1	240.8	4.7	4
Q3a	ESE	110-Ch.1-FIA6	P	2.7	2.2	2.5	0.2	6	250.2	243.3	245.9	2.8	5
Q3b	E	102a-Ch.1.a-FIA1	P	4.7	3.6	4.3	0.5	5	277.2	264.2	270.7	9.2	2
Q3b	E	102a-Ch.1.a-FIA2	P	3.7	3.6	3.7	0.1	4	252.0	246.4	249.2	4.0	2
Q3b	E	102a-Ch.1.a-FIA3	P	4.8	4.3	4.6	0.2	5	262.3	247.5	255.2	7.2	5
Q3b	E	102a-Ch.1.a-FIA4	P	3.7	3.6	3.6	0.1	5	170.7	167.8	169.6	1.1	6
Q3b	E	102a-Ch.1.a-FIA5	PS	3.6	3.6	3.6	0.0	3	253.7	244.9	249.3	6.2	2
Q3b	E	102a-Ch.1.a-FIA6	P	3.4	3.2	3.3	0.1	4					
Q3b	E	102a-Ch.1.a-FIA7	PS	3.7	2.3	3.4	0.2	5					
Q3b	E	102a-Ch.1.a-FIA8	P	3.6	3.6	3.6	0.0	5					
Q3b	E	102c-Ch.1-FIA1	P	4.3	4.2	4.3	0.1	5	256.0	252.7	254.4	1.4	4
Q3b	E	102c-Ch.1-FIA2	P	4.2	3.9	4.1	0.2	6	250.5	247.9	249.0	1.3	3
Q3b	E	104a-Ch.1.a-FIA1	P	6.3	4.5	5.4	0.9	6	225.3	213.6	219.5	8.3	2
Q3b	E	104a-Ch.1.a-FIA2	P	4.8	4.2	4.5	0.2	6	250.5	242.1	247.0	3.9	5
Q3b	ESE	106-FIA1	P						169.9	165.6	167.4	2.2	3
Q3b	ESE	106-FIA2	P	2.2	2.1	2.2	0.1	4	208.6	194.6	200.5	7.2	3
Q3b	ESE	106-FIA3	PS	2.1	1.9	2.0	0.1	5	221.6	218.5	220.3	1.6	3
Q3b	ESE	108a-FIA2a	PS	1.9	1.7	1.8	0.1	5	206.3	201.6	203.5	2.5	3
Q3b	ESE	108a–FIA2b	PS	1.9	1.7	1.9	0.1	5	192.1	185.1	187.9	3.0	4
Q3b	ESE	108a–FIA3	P	3.1	2.9	3.0	0.1	8	181.2	175.0	178.4	2.1	6

Table 3 (continued)

Mineral	Vein segment	Sample #	FIA type	Salinity wt% NaClequiv.					Th (°C)				
				Max	Min	Avg.	SD	*n*	Max	Min	Avg.	SD	*n*
Q4a	L	114-Ch.1-FIA1	P						202.4	184.3	193.7	7.4	3
Q4a	L	114-Ch.1-FIA3	P	4.3	4.3	4.3	0.0	2	199.7	185.3	190.8	7.8	3
Q4a	E	103a-Ch.1-FIA2	P	4.7	4.3	4.6	0.1	6	215.6	210.9	214.1	1.6	6
Q4a	E	103a-Ch.1-FIA3	P	5.1	4.7	4.9	0.2	6					
Q4a	E	103a-Ch.1-FIA4	P	4.5	4.3	4.5	0.1	8	214.3	210.6	212.2	1.6	7
Q4b	E	103a-Ch.2-FIA1	PS	2.2	1.9	2.1	0.2	3	217.4	205.7	212.5	6.1	3
Q4b	E	103a-Ch.2-FIA2	P	1.4	1.2	1.3	0.1	3			205.9	0.0	1
Q4b	E	103c-Ch.1-FIA1	P	2.1	1.7	2.0	0.2	4	206.0	201.6	204.6	2.0	4
Q4b	E	103c-Ch.1-FIA2	P	2.1	1.9	2.0	0.1	4	215.3	212.8	213.9	1.1	4
Q4b	E	103c-Ch.1-FIA3	PS	2.2	2.1	2.1	0.1	7	213.1	206.6	210.4	2.7	6
Q4b	E	103c-Ch.1-FIA4	PS	2.7	1.4	2.1	0.6	5	212.4	206.8	209.3	2.3	4
Q4b	E	103c-Ch.1-FIA5	P	2.1	2.1	2.1	0.0	6	212.7	205.3	209.3	2.9	6
Q4b	E	103c-Ch.1-FIA7	P	2.4	2.2	2.3	0.1	8	191.0	173.9	182.5	7.3	7
Q4b	E	103c-Ch.2-FIA1	P	4.7	4.5	4.6	0.1	9	224.8	223.9	224.4	0.4	9
Q4b	E	103c-Ch.2-FIA2	P	4.7	4.3	4.5	0.1	9	212.6	205.3	208.6	2.4	6
Q4b	E	103c-Ch.2-FIA3	P	4.3	4.2	4.3	0.1	7	262.9	261.9	262.4	0.5	3
Q4b	E	103c-Ch.2-FIA4	PS	4.7	4.2	4.5	0.2	8	211.4	210.4	210.8	0.3	7
Q4b	E	103c-Ch.2-FIA5	P	4.2	3.9	4.1	0.1	9	271.4	264.5	268.6	2.0	9
Q4b	E	103c-Ch.2-FIA6	PS	5.0	4.5	4.7	0.2	8	220.0	214.7	217.7	1.8	7
Q4b	E	103c-Ch.2-FIA7	P	4.5	4.2	4.4	0.1	8	183.9	180.9	182.2	1.5	3

(Rauchenstein-Martinek et al. 2014). Limits of detection can be calculated for each element in each inclusion (Longerich et al. 1996; extended for small count numbers by Pettke et al. 2012), but estimating an upper limit for an element concentration in an assemblage is ambiguous. Normalisation of background-corrected counts for a trace element to those of Na (used as internal standard for calculating absolute concentrations; Günther et al. 1998; Heinrich et al. 2003) means that a high LOD for a trace element concentration primarily reflects a low Na signal (e.g. due to small inclusion size). Therefore, averaging all LODs in an FIA overestimates the likely maximum concentration of the element in the palaeo-fluid represented by the FIA. On the other hand, taking the lowest of all calculated detection limits in the FIA under-estimates the likely upper limit on possible trace element concentration, because it ignores the fact that the small signals themselves have considerable statistical uncertainty. In Table 4, the '< values' report a semi-quantitative estimate of the likely upper concentration limit, based on inspection of results from several of the best and largest inclusions in each assemblage. The variability of small signals also means that peaks identified as clearly detected according to statistical criteria (Pettke et al. 2012) tend to be biased towards the larger signals in a random population, whereas the randomly smaller signals fall below the detection criterion. Using large statistical datasets of up to 100 inclusions in one assemblage, Rauchenstein-Martinek et al. (2014) showed that averaging a small fraction of detected element concentrations for gold in a homogeneous FIA may lead to a tenfold overestimation of the true gold content of the fluid. In the present study, we only found a small number of measureable inclusions in each assemblage. Nevertheless, critical inspection of results as shown below allows an estimate of the concentrations of gold that was transported in the ore fluid.

Mineralogy of the Alto de la Blenda vein system

The general paragenetic sequence (Fig. 5) of the deposit is complex with several stages of renewed vein opening and brecciation, but timing relations of petrographically similar assemblages can be tentatively correlated between several sites of detailed outcrop mapping, as illustrated in Figs. 6 and 7.

We identified four stages of hydrothermal mineralisation that can be consistently recognised in many areas of the Alto

Table 4 Average LA–ICP–MS analyses of fluid inclusion assemblages in quartz and sphalerite from Alto de la Blenda (concentrations in μg/g; upper limits marked by '<' symbols are estimated from individual limits of detection)

Mineral	Vein segm.	Sample #	Number of samples	FI type	Na	S	K	Fe	Cu	As	Ag	Sb	Cs	Au	Pb
Qp	ESE	301-1a-FIA1	4	P	8700	620	4000	250	390	9	<2.5	1	10	<0.2	20
Qp	ESE	301-1a-FIA2	8	P	7100	3100	4500	1330	340	40	10	15	30	0.7	50
Qp	ESE	301-1a-FIA3	4	P	7700	<2800	2300	1180	180	200	1	<1	20	<0.4	140
Qp	ESE	301-1a-FIA4	6	P	33,300	<19,000	16,000	6530	140	50	30	40	180	0.3	570
Q1	L	122.a-Ch.2-FIA1	4	P	4000	<7000	9200	3290	170	180	15	30	10	<2.2	25
Q1	L	122.a-Ch.2-FIA2	5	P	7000	<3000	2100	5960	50	40	1	15	10	3.3	20
Q1	L	122.a-Ch.2-FIA3	3	P	6900	1280	3300	<700	10	25	10	40	10	<1	5
Q1	L	122.a-Ch.5-A1-FIA1a	2	PS	10,400	<1000	2700	<500	40	<15	3	<4	10	<0.6	<3
Q1	L	122.a-Ch.5-A1-FIA1b	3	PS	10,100	<1000	1700	<600	30	<15	3	<4	5	<0.4	5
Q1	L	122.a-Ch.5-A1-FIA2	5	PS	7700	<10,000	11,200	4950	250	500	25	25	20	2.6	70
Q1	L	122.a-Ch.5-A2-FIA1	1	P	7600	<460	1500	<250	<5	<8	<1	4	10	<0.2	<1
Q1	E	105-Chip 2-FIA3	1	P	9700	<1800	7600	n.a.	340	n.a.	n.a.	n.a.	10		<12
Q2a	L	001(G)-FIA1	5	P	7300	<8000	5200	6590	1530	n.a.	n.a.	n.a.	80	1.8	120
Q2a	L	001(G)-FIA2	3	P	5200	7670	6900	11,580	420	n.a.	n.a.	n.a.	30	<2.8	290
Q2a	L	001(R)-FIA1	1	P	7300	<44,000	3400	<10,000	<160	<350	<35	<81	<20		900
Q2a	L	001(R)-FIA2	2	PS	7500	<3000	7800	2290	90	n.a.	n.a.	n.a.	25	2.7	55
Q2a	L	122.a-Ch.5-A1-FIA3	1	P	4300	<7000	16,200	<4000	460	690	25	120	25	<2.0	<17
Q2a	E	101.b-Ch.1a-FIA1	6	P	7700	10,070	20,000	11,470	410	880	<60	360	30	<1.3	140
Q2a	E	105-Ch.2-FIA1	1	P	14,000	<3000	2000	n.a.	150	n.a.	n.a.	n.a.	230	3.7	<20
Q2a	E	105-Ch.2-FIA2	1	P	11,200	<5000	11,300	n.a.	<50	n.a.	n.a.	n.a.	20		<36
Q2a	E	105-Ch.2-FIA4	1	P	12,000	<200	2100	n.a.	5	n.a.	n.a.	n.a.	10	<0.4	3
Q2b	L	122.b-Ch.2-FIA1	5	PS	10,100	<1900	3400	670	20	40	1	40	10	0.6	5
Q2b	L	122.b-Ch.2-FIA3	5	P	7500	65	1700	<500	120	30	3	30	10	0.1	3
Q2b	L	122.b-Ch.2-FIA4	2	P	9900	<2600	3200	2900	60	250	<2.4	450	10	<0.6	10
Q2b	E	003-A.8-FIA5	10	P	13,700	13,440	4700	5710	340	<300	<35	<10	30	6.3	45
Q2b	E	105-Ch.1-FIA1	1	P	13,200	4500	<1000	<4500	<250	n.a.	n.a.	n.a.	40	14.4	<30
Q2b	E	105-Ch.1-FIA2	2	P	13,300	<2300	1100	9900	230	n.a.	n.a.	n.a.	5	1.0	<3
Q2b	ESE	132-Ch.2-FIA1	4	P	9200	<200	1100	<85	<3	15	0.2	12	10	0.1	2
Q2b	ESE	132-Ch.2-FIA2	2	PS	8300	<250	2700	250	<4	6	<0.5	0.3	5	0.1	<1
Q2b	ESE	132-Ch.2-FIA4	4	P	10,500	1060	600	30	<2	6	0.0	12	1	<1	0
Sp2	E	35-Ha-FIA1	5	P	4300		2600			10	30	25	6	<0.9	20
Sp2	E	35-Ha-FIA2	7	P	6600		3700			10	60	25	5	0.9	230
Q3a	L	024-B1-FIA4	1	P	12,800	<2000	900	<700	<20	25	<1.5	45	10	<1.7	8
Q3a	E	103.b-FIA1	4	PS	13,700	<3000	4100	300	400	n.a.	n.a.	n.a.	25	1.3	10
Q3a	E	127-Ch.5-FIA3	2	PS	5300	<1200	1800	1000	<10	<10	<2	4	5	<0.9	4
Q3a	E	127-Ch.5-FIA5	1	P	5800	4700	<7000	<6500	<200	510	73	<50	110	<12.6	230
Q3a	E	127-Ch.5-FIA6	8	P	4500	5250	2900	<1300	65	10	10	50	10	1.0	20
Q3a	E	127-Ch.5-FIA7	5	P	8000	290	3300	1170	10	25	<5	40	20	<2.8	26
Q3a	ESE	110-Ch.1-FIA1	3	P	7500	910	1000	2850	90	50	0	120	5	<0.8	7
Q3a	ESE	110-Ch.1-FIA4	1	PS	14,200	910	2800	<2500	<75	<50	<7	<30	30	<3.9	<10
Q3a	ESE	110-Ch.1-FIA6	2	P	9300	90	1000	6	0	40	0	20	5	0.0	0
Q3b	E	102a-Ch.1.a-FIA2	2	P	13,000	6720	1900	700	950	n.a.	n.a.	n.a.	40	3.3	97
Q3b	E	102a-Ch.1.a-FIA3	2	P	16,600	<2300	2500	4400	330	n.a.	n.a.	n.a.	25	2.3	<3.5
Q3b	E	102a-Ch.1.a-FIA4	3	P	12,000	3320	3800	3670	950	n.a.	n.a.	n.a.	40	8.8	73

Table 4 (continued)

Mineral	Vein segm.	Sample #	Number of samples	FI type	Na	S	K	Fe	Cu	As	Ag	Sb	Cs	Au	Pb
Q3b	E	102a-Ch.1.a-FIA5	3	PS	12,200	<5000	6700	1610	360	n.a.	n.a.	n.a.	35	1.2	20
Q3b	E	102a-Ch.1.a-FIA6	2	P	10,700	<2200	4600	720	270	n.a.	n.a.	n.a.	25	<1.7	7
Q3b	E	102a-Ch.1.a-FIA7	4	PS	9600	5400	6500	1030	340	n.a.	n.a.	n.a.	10	9.9	75
Q3b	E	102a-Ch.1.a-FIA8	3	P	13,100	<600	2200	<200	70	n.a.	n.a.	n.a.	10	1.4	<1
Q3b	E	102c-Ch.1-FIA1	7	P	14,300	<11,800	12,000	n.a.	70	n.a.	n.a.	n.a.	35	2.5	140
Q3b	E	102c-Ch.1-FIA2	7	P	13,800	1270	7700	n.a.	5	n.a.	n.a.	n.a.	45	2.3	70
Q3b	E	104a-Ch.1.a-FIA1	1	P	14,800	<5000	<4000	<1600	4470	n.a.	n.a.	n.a.	240		<100
Q3b	E	104a-Ch.1.a-FIA2	13	P	15,500	6010	7300	2300	105	660	7	220	20	5.1	65
Q3b	ESE	108a-FIA2a	1	PS	5900	<60	1600	<30	<1	200	<1	720	10	<0.1	<1
Q3b	ESE	108a–FIA2b	5	PS	6300	120	1700	40.0	3	300	2	610	10	0.1	1
Q3b	ESE	108a–FIA3	3	P	10,800	3700	3000	<400	30	140	1	340	10	0.9	<2
Q4a	L	114-Ch.1-FIA1	7	P	4000	1340	2300	190	90	15	4	30	10	0.6	0
Q4a	L	114-Ch.1-FIA3	3	P	12,700	2200	3400	770	75	<22	7	90	20	<1	3
Q4a	E	103a-Ch.1-FIA2	1	P	18,300	<4000	<300	<1000	<100	n.a.	n.a.	n.a.	5	2.0	<8
Q4a	E	103a-Ch.1-FIA3	4	P	15,000	4650	12,500	950	540	n.a.	n.a.	n.a.	20	0.7	52
Q4a	E	103a-Ch.1-FIA4	3	P	14,900	670	7500	2970	595	n.a.	n.a.	n.a.	10	1.0	22
Q4b	E	103c-Ch.1-FIA3	9	PS	7300	2860	2900	2500	110	20	1	14	10	<0.8	20
Q4b	E	103c-Ch.2-FIA1	4	P	15,100	7170	5200	950	80	n.a.	n.a.	n.a.	25	2.2	22
Q4b	E	103c-Ch.2-FIA3	4	P	14,300	7730	2800	5370	240	n.a.	n.a.	n.a.	15	<2.5	23
Q4b	E	103c-Ch.2-FIA5	6	P	12,500	<2300	2600	1950	1065	n.a.	n.a.	n.a.	30	2.1	52
Q4b	E	103c-Ch.2-FIA6	6	PS	14,700	5230	4600	15,200	1660	n.a.	n.a.	n.a.	35	<1.8	30
Q4b	E	103c-Ch.2-FIA7	7	P	15,400	4840	3300	2240	260	n.a.	n.a.	n.a.	15	1.3	10

de la Blenda vein system. Figure 6 shows two detailed outcrop maps, in which successive events of vein opening and precipitation of layers of characteristic hydrothermal minerals, notably distinctly coloured and textured carbonate types, can be tentatively correlated between locations in the Laboreo segment (Fig. 6a) and the Esperanza segment in the centre of the Alto de la Blenda vein system (Fig. 6b). All four stages of hydrothermal mineral precipitation are dominated by quartz and carbonates, which comprise >90 % of the vein volume in comparable proportion. Pyrite is the most abundant and widespread sulphide mineral. Base metal-bearing minerals occur in the last three stages (2 to 4), and precious metal-bearing minerals are associated with stages 2 and 3 only, as summarised in Fig. 5. Representative ore mineral compositions are reported in Tables 1 and 2.

In several areas of the deposit, localised brecciation affects different parts of the sequence. In some areas, these breccias show a comprehensive history of the deposit, where all stages can be recognised, including the relations between vein stages pre- and postdating the polymictic breccia containing fragments of sphalerite–galena–carbonate veins (stage 2) and earlier porphyries with quartz phenocrysts and isolated clear quartz fragments (Qp; Fig. 7a, b) as well as later vein stages 3 and 4 cutting the contact of the polymictic breccia (Fig. 7e).

Gangue minerals

The gangue minerals quartz and carbonates are described first, in light of their abundance and distinctive characteristics that help in identifying and correlating of the stages of mineralisation. Adularia is conspicuously absent from all vein stages.

Quartz We identified four generations of quartz, each having different appearance and abundance. The first generation (quartz 1 (Q1)) is medium to light grey in colour, sometimes with a bluish hue, massive and granular with a small grain size (<1 mm). It hosts myriads of fluid inclusions that are in general <1 μm in size. Q1 occurs closely associated with the first generation of carbonates and pyrite, in scattered fragments (Fig. 7c) that show evidence of two or three later brecciation episodes. The second generation of quartz (Q2) occurs as the first mineral cementing fragments of stage 1 (Fig. 7c) and in thin veinlets (<1 cm). It is associated with a second generation of carbonates and pyrite, and the earliest base and precious

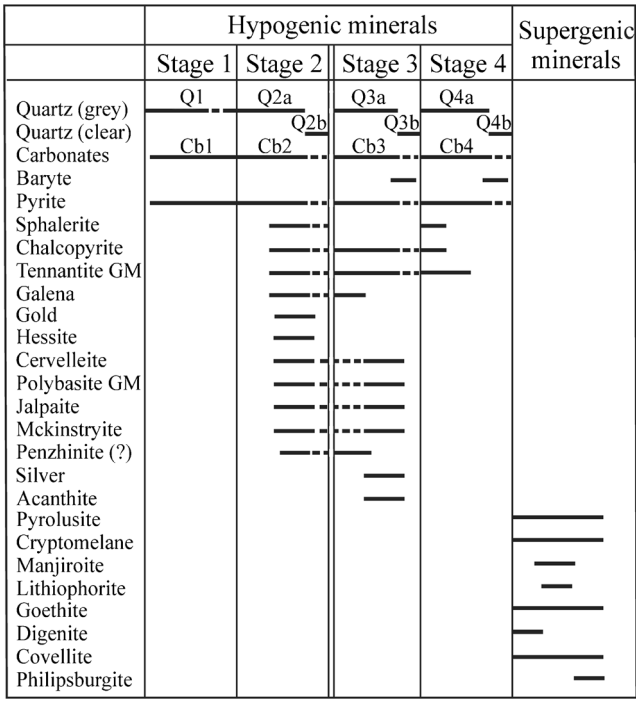

Fig. 5 Alto de la Blenda paragenetic sequence derived primarily on successive generations of characteristic carbonate types and quartz textures alternating from massive (Q1, Q2a to Q4a) to coarse and locally vuggy (Q2b to Q4b). The vertical separation between stages 2 and 3 shows the interpreted time of emplacement of the hanging wall breccia (Fig. 4b), a polymictic pebble dyke containing fragments brought up from greater depth as well as vein fragments resembling stages 1 and 2 of the local vein

metal-bearing minerals. This quartz is grey in colour and translucent and its grain size is ≤1 mm (Q2a). Towards the end of this stage, it develops clear to colourless crystals (Q2b) up to 2 or 3 mm long that grow in small cavities. The third generation (Q3a and b) is similar to Q2 in many aspects such as size and colour and the tendency to develop transparent, colourless crystals that reach up to 2 cm in size and develop comb textures. It is accompanied (Fig. 7c–e) by the third generation of carbonates (Cb3). Ore mineral assemblages are similar to the previous stage 2, but only Ag is in the precious metal-bearing minerals. Quartz postdating all previous generations (Q4a and b) is similar to Q2 and Q3 in its appearance, but it is less abundant and paragenetically related to the fourth generation (Cb4) of carbonates (Fig. 7e), pyrite and base metal-bearing minerals; no precious metal-bearing minerals were identified in this stage.

Carbonates —$(Ca,Mn^{2+})CO_3$ and $(Mn^{2+},Ca)CO_3$—are present as white, cream to yellowish calcite, pinkish white Mn-rich calcite and pale pink, Ca-rich rhodochrosite. The first generation of carbonates (Cb1) occurring with Q1 is volumetrically minor in most places, creamy to pink in colour (Fig. 7c) and is associated with disseminated pyrite. In stage 2, the carbonates (Cb2) occur interlayered with Q2 (Fig. 7c) and the bands of this creamy carbonate are associated with free Au and various sulphide and sulphosalt minerals. The third generation of carbonates (Cb3) is pink to yellowish and occurs associated with Q3 (Fig. 7c–e), chalcopyrite and Ag-bearing sulphosalts. Cb4 represents the last generation of carbonates identified in the Alto de la Blenda veins and is mainly white to pink, in banded veinlets (Fig. 7e) and associated with scarce pyrite, chalcopyrite, sphalerite and tennantite. Locally, the association Q4a+Cb4 is parallel to bands of earlier stages, but it was also found crosscutting it (Figs. 6b and 7e). In several areas of the deposit, localised brecciation affects different parts of the sequence. Carbonates from all stages show massive, columnar and crustiform textures; bladed textures were not observed.

Baryte is scarce and occurs in tabular crystals, generally associated with Q4 and Cb4, but is also rarely found with Q3 and Cb3.

Supergene Mn oxides and hydroxides are dominantly cryptomelane $[K(Mn^{4+},Mn^{2+})_8O_6]$ and pyrolusite $[Mn^{4+}O_2]$, and subordinate manganite $[Mn^{3+}O(OH)]$, manjiroite $[(Na,K)(Mn^{4+},Mn^{2+})_8O_{16}{\cdot}nH_2O]$ and 'wad'. Carbonate oxidation varies from incipient (Fig. 7f) to pervasive (Fig. 7g), and most of the surfaces, unless freshly mined, are covered by a Mn oxide patina that at first sight gives the impression that the carbonates are totally replaced.

Hypogene ore minerals

The hypogene ore minerals are described in order of their appearance in the paragenetic sequence.

Pyrite occurs as the earliest sulphide in stage 1, but it formed in all four stages of mineralisation. It occurs as subhedral to anhedral, up to 500-μm crystals in quartz and also as tiny crystals disseminated in calcite. Pyrite is partly replaced by sphalerite, chalcopyrite and galena, locally following growth lines (Fig. 8a) and oxidised in different degrees to goethite. Three EMP analyses of pyrite (one listed in Table 1) gave consistently low As contents of 0.19 ± 0.02 wt% but variably high Au concentrations of 0.07, 0.19 and 0.53 wt%, which are well above the limit of Au^+ incorporation into arsenian pyrite (Reich et al. 2005) and indicate that some of the gold is present as nanoparticles enclosed in pyrite (Deditius et al. 2011).

Sphalerite occurs as subhedral to anhedral, up to 5-mm crystals, disseminated in quartz or carbonates and associated with pyrite, galena and quartz, also developing one or two sets of

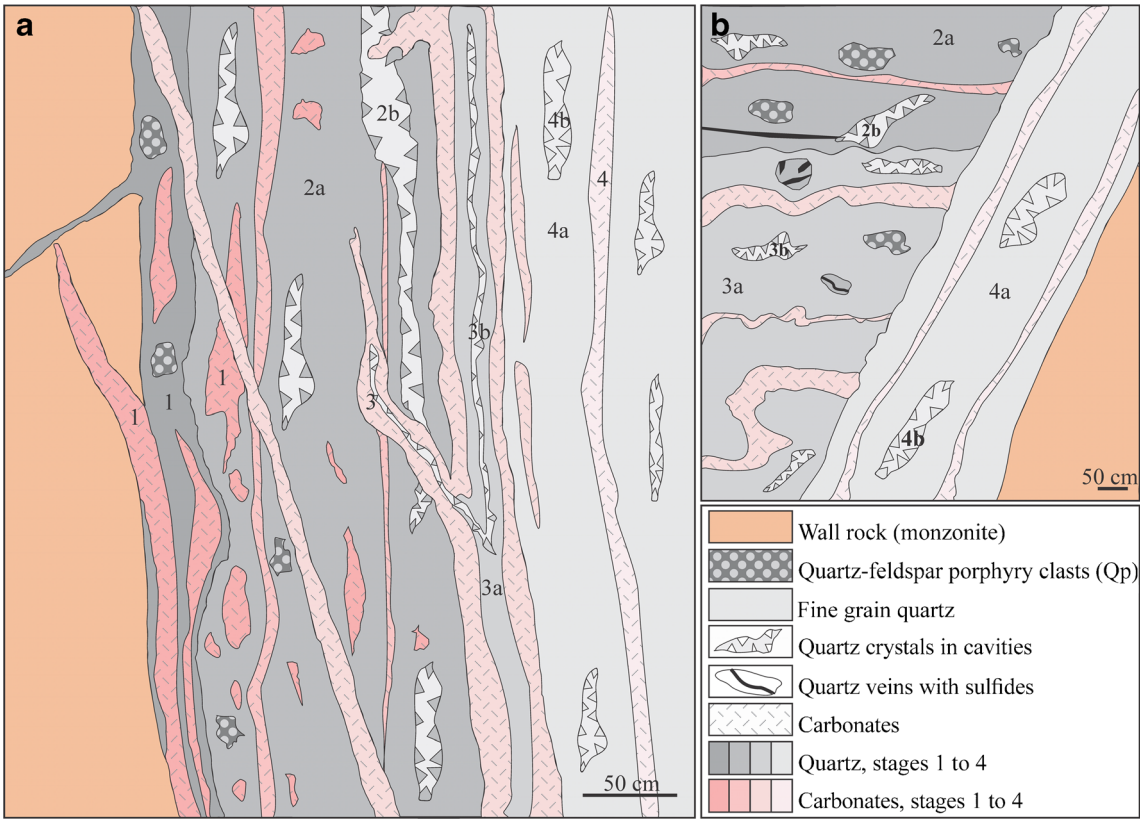

Fig. 6 Two representative outcrop maps showing repeated brecciation and four stages of hydrothermal vein mineralisation that can be correlated between different vein segments. *Colour shades* from *dark* to *light* indicate successively younger stages; *patterns* indicate recurrences of the same minerals. **a** Laboreo segment, −208 level. **b** Esperanza segment, −120 level. *Scale bar*, 50 cm

discontinuous veinlets from less than 5 μm, up to 1 to 2 cm crisscrossing the carbonates. Its colour and transparency varies in different specimens and even in the same crystal from totally opaque, dark brown to almost transparent with colourless, yellow and light yellowish-brown colour and numerous fluid inclusions (Fig. 8b); commonly, the crystals have a yellow core with ≤0.004 Fe atoms per formula unit (apfu) surrounded by a darker rim with up to 0.055 Fe apfu, which could suggest that the fluids evolved from higher to lower sulphidation potential (Scott and Barnes 1971; Einaudi et al. 2003). There are two generations of this mineral (Sp2 and Sp4) that occur in stages 2 and 4, respectively. Fragments of sphalerite belonging to the second stage of the mineralisation (Sp2) were found in the hanging wall breccia in Esperanza and Esperanza NE segments. The ore minerals associated with Sp2 are chalcopyrite, galena, native Au and sulphosalts, whereas chalcopyrite and tennantite accompany Sp4. Both generations of sphalerite coexist with and partly replaces pyrite (Fig. 8a). Table 1 shows two representative EMP analyses of the core: Sp2(c) and border: Sp2(b) of a crystal of sphalerite from stage 2; the Fe content does not show a significant difference in the two generations of sphalerite; the highest measured Fe value (3.18 wt%, 0.055 apfu) corresponds to the border of a crystal of sphalerite of stage 2, but the analyses shown in Table 1 correspond to sphalerite of that same stage, showing much lower contents of Fe. Indium was always below the detection limit of ~400 ppm.

Chalcopyrite was identified in three generations, which crystallised in stages 2 and 3 and during the first part of 4. It occurs disseminated in anhedral to subhedral crystals (<2 to 500 μm, avg. 20 μm) or in millimetre-sized, irregular patches (Fig. 8c), mainly in quartz, associated with pyrite, sphalerite, galena and gold. This mineral also develops some discontinuous veinlets, up to 400 μm wide (50 μm in average), in sphalerite and local trends of crystals in galena. Chalcopyrite disease in sphalerite is common, generally developing dusted and watermelon textures. This mineral is replaced by covellite in different degrees. A representative EMP analysis is shown in Table 1; in a few analyses, minor contents of Pb, Mn and Zn were detected.

Tennantite-group minerals Tetrahedrite and tennantite occur in stages 2, 3 and 4. They are present in small grains, generally <40 μm, mainly in quartz and associated with sphalerite, chalcopyrite, galena and hessite. Some of the

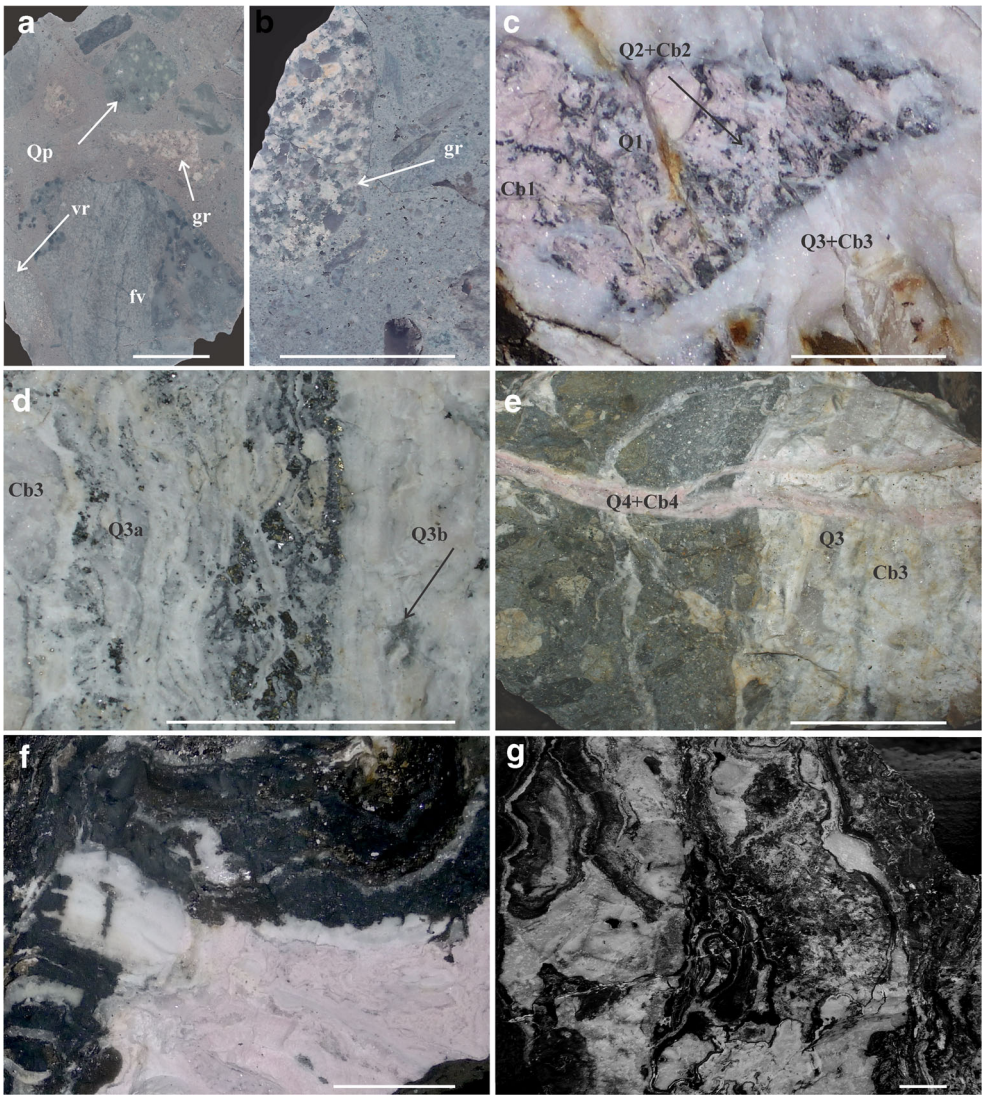

Fig. 7 Photographs showing different stages of mineralisation. **a**, **b** Hanging wall breccia with clasts of porphyry (*Qp*), muscovite granite (*gr*), felsic volcanic rocks (*vr*) and fragments of veins (possibly belonging to stage 2 because galena and minor sphalerite were recognised (*fv*)). **c** Two-stage breccia with fragments of *bluish grey* quartz (*Q1*), *pink* carbonate (*Cb1*; partly stained black by oxidation) and scarce disseminated pyrite, cemented by a second generation of *grey* quartz (*Q2*) after stage 2 brecciation, all occurring in a clast surrounded by a third generation of *grey* quartz (*Q3a*) + pale carbonate (*Cb3*), following another brecciation event. **d** *Grey* quartz (*Q3*) associated with *light pink* to *yellowish* carbonate (Cb3) and ore minerals occur parallel to the breccia. **e** Veinlet of minor quartz (Q4) and *pink white*-layered carbonate (Cb4) crosscuts the previous sequence on the steep contact to the hanging wall breccia. **f** Incipient supergene oxidation, showing an irregular but sharp front controlled in part by hypogene banding. **g** Carbonates completely replaced by Mn oxides, preserving quartz (*white*) and original vein structure. All *scale bars*, 3 cm

grains are partially replaced by digenite. Certain grains are zoned, as evident under the electron microprobe, with alternating bands of tetrahedrite and tennantite (Fig. 8d). A representative EMP analysis for each species is shown in Table 2, and the empirical formulae calculated on the basis of 29 atoms per formula unit for tetrahedrite and tennantite are, respectively, as follows: $(Cu_{5.75}Ag_{0.23})_{\sum 5.98}Cu_{4.00}(Zn_{1.84}Fe_{0.21})_{\sum 2.05}(Sb_{3.52}As_{0.78})_{\sum 4.30}S_{12.67}$ and $(Cu_{5.29}Ag_{0.47})_{\sum 5.76}Cu_{4.00}(Zn_{1.54}Fe_{0.50})_{\sum 2.04}(As_{3.60}Sb_{0.40})_{\sum 4.00}S_{13.20}$. Some analyses of tetrahedrite showed the presence of minor quantities (up to 0.35 wt%) of Ga, Se, Cd, Sn and Tl, whereas in tennantite, only Sn in small amounts (0.08 wt%) was found.

Galena occurs in subhedral micro- to millimetre-sized crystals disseminated in calcite and quartz. This mineral is more or less contemporaneous to slightly later than sphalerite and, in some areas, develops skeletal textures, indicating relatively fast crystal growth. Some galena fills open spaces in cracked pyrite and has inclusions of hessite. Galena is partly replaced by cerussite, generally following cleavage planes. The EMP analyses show a stoichiometric composition, and a representative chemical analysis is shown in Table 1. Silver is present in some samples with up to 1.5 wt%, plus minor contents of Cu, Fe, Zn and Mn; in one sample, we detected 0.24 wt% thallium.

Gold (electrum) mainly occurs in the second stage of the mineralisation but was never observed macroscopically. It is disseminated as irregular grains (<1 μm up to 60 μm) in quartz, calcite, pyrite and chalcopyrite (Fig. 8c). Gold has a variable fineness, from 782 to 650 averaging 695. EMP analyses also show Cu up to 0.41 wt% (average 0.13 %).

Two telluride minerals were found: hessite and cervelleite. *Hessite* is rarely found in subhedral, tabular to rounded grains

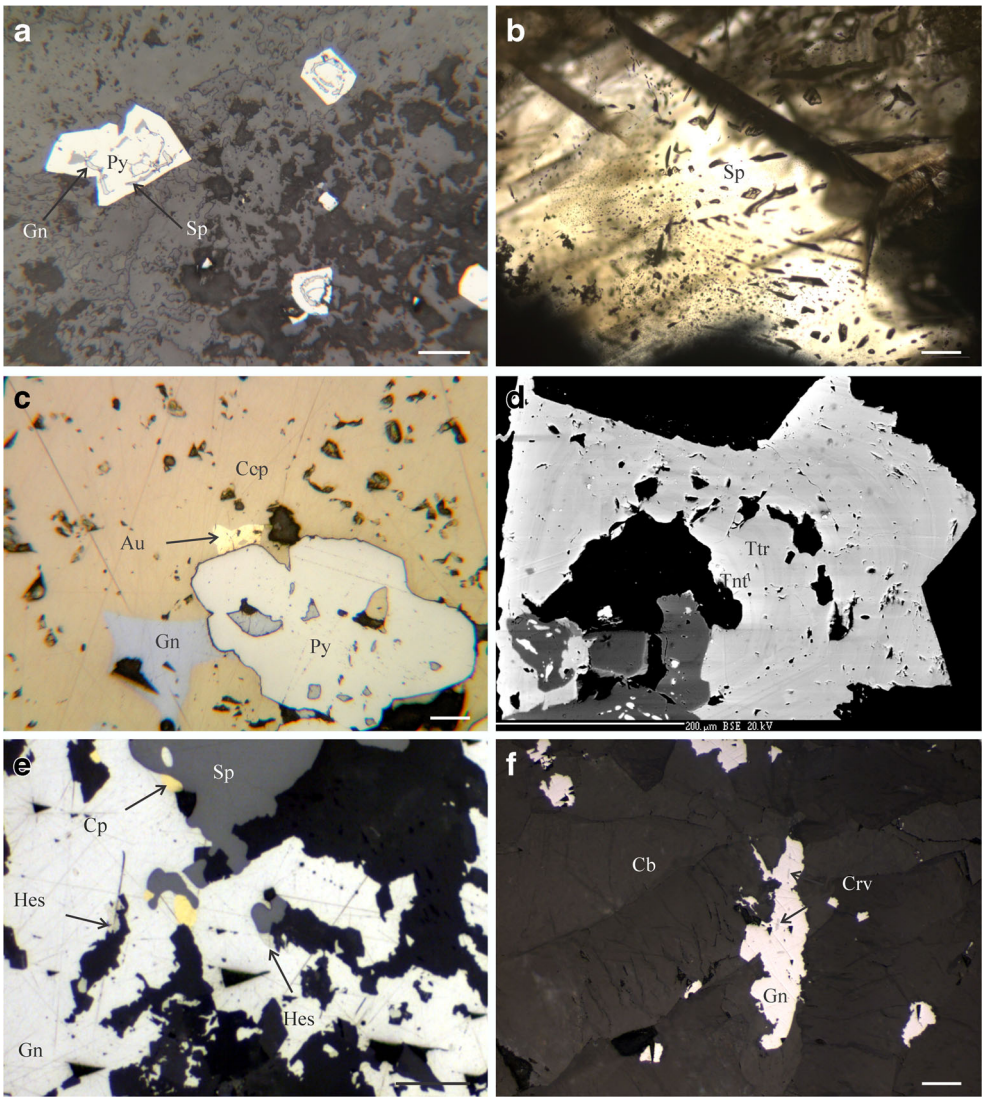

Fig. 8 **a**, **b**, **c**, **e**, **f** Photomicrographs and **d** BSE image of typical mineral assemblages. **a** Pyrite (*Py*) partly replaced by sphalerite (*Sp*) and galena (*Gn*), locally following fracture planes or growth surfaces. **b** *Light yellowish brown* to *dark brown* sphalerite with numerous fluid inclusions. **c** Chalcopyrite (*Ccp*) associated with pyrite, galena and gold (*Au*). **d** Alternating bands of tetrahedrite (*Ttr*) and tennantite (*Tnt*). **e** Hessite (*Hes*) in galena associated with sphalerite and chalcopyrite. **f** Cervelleite (*Crv*) associated with galena, included in carbonates (*Cb*). *Scale bar* in photomicrographs, 50 μm. Mineral abbreviations largely following Whitney and Evans (2010)

in galena associated with chalcopyrite and sphalerite (Fig. 8e) and with tennantite; its empirical formula calculated from the representative EMP analysis shown in Table 1 is $Ag_{1.98}Te_{1.02}$. *Cervelleite* occurs as very scarce, small (5 to 20 μm) anhedral blebs in galena (Fig. 8f); Table 1 shows a representative EMP analysis giving the empirical formula $(Ag_{3.78}Cu_{0.17}Zn_{0.04})_{\sum 3.99}Te_{1.07}S_{0.94}$.

Polybasite-group minerals The species of this group of minerals identified in Alto de la Blenda are pearceite, polybasite, cupropearceite and cupropolybasite (Table 2). All are scarce, especially the latter two. These minerals commonly coexist in the same sample and are very similar in reflected light; they were identified with EMP analyses. Pearceite occurs in irregular grains up to 100 μm across, associated with galena and gold and partially replaced by acanthite. Its average empirical formula is $[(Ag_9CuS_4)][(Ag_{4.51}Cu_{1.48})_{\sum 5.99}(As_{1.52}Sb_{0.42})_{\sum 1.94}\ S_{7.09}]$.

Polybasite is generally included in galena (Fig. 9a) as anhedral, rounded grains, with an average size of 50 μm, that locally occurs with chalcopyrite. The average empirical formula is $[(Ag_9CuS_4)][(Ag_{4.85}Cu_{1.22})_{\sum 6.07}\ (Sb_{1.19}As_{0.72})_{\sum 1.91}(S_{6.78}Te_{0.24})_{\sum 7.02}]$. Cupropearceite occurs as irregular grains (<50 μm) included in quartz and partially replaced by acanthite (Fig. 9b) and in some areas replaced by digenite ± covellite. Its empirical formula is $[(Ag_9CuS_4)][(Cu_{3.27}Ag_{2.71}Zn_{0.05})_{\sum 6.03}(As_{1.38}Sb_{0.62})_{\sum 2.00}\ S_{6.97}]$. Cupropolybasite occurs as isolated grains included in quartz and locally intergrown with Cu-rich mckinstryite (Fig. 9c), and its average empirical formula is $[(Ag_9CuS_4)][(Cu_{4.19}Ag_{1.57}Zn_{0.33})_{\sum 6.09}\ (Sb_{1.17}As_{0.81})_{\sum 1.98}S_{6.93}]$.

Silver–copper sulphides are scarce but varied (Table 1) and include *acanthite* partially replacing the polybasite-group minerals and mckinstryite (Fig. 9b, c). EMP analyses show a composition close to stoichiometric $Ag_{2.00}S_{1.00}$.

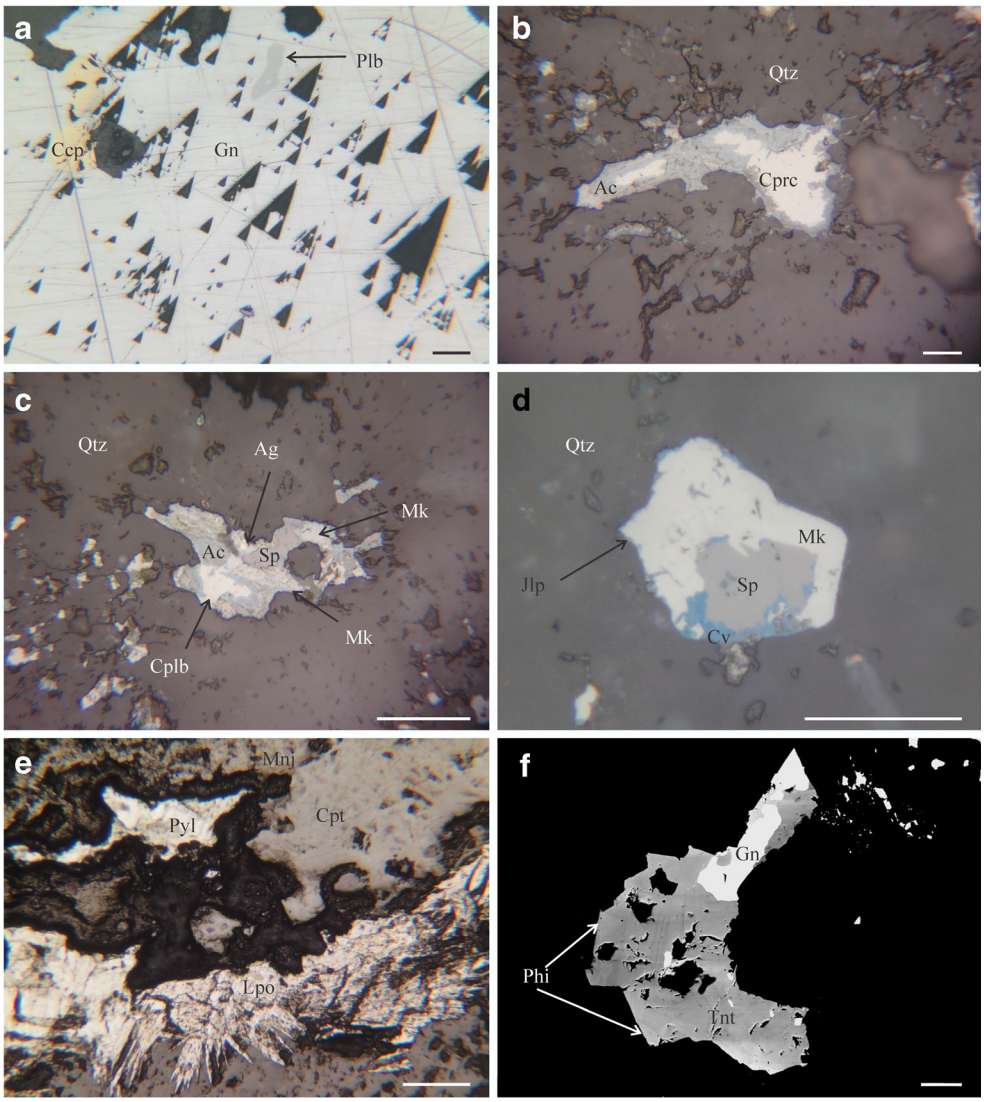

Fig. 9 **a**, **b**, **c**, **d**, **e** Photomicrographs and **f** BSE image (all *scale bars*, 50 μm). **a** Polybasite (*Plb*) included in galena. **b** Cupropearceite (*Cprc*) included in quartz and partially replaced by acanthite (*Ac*). **c** Isolated grains of cupropolybasite (*Cplb*) intergrown with Cu-rich mckinstryite (*Mk*) and minor sphalerite and silver (*Ag*) included in quartz and partially replaced by acanthite. **d** Jalpaite (*Jlp*) disseminated in quartz, associated with mckinstryite and sphalerite, and partly replaced by covellite (*Cv*). **e** Patches of supergene oxidation with cryptomelane (*Cpt*), pyrolusite (*Pyl*) and manjiroite (*Mnj*), associated with radiated fibrous crystals of lithiophorite (*Lpo*). **f** Grain of tennantite, with inclusions of galena, and small grains of philipsburgite (Phi) at its borders

Jalpaite occurs as irregular grains up to 40 μm across in quartz, associated with mckinstryite and sphalerite and partly replaced by likely supergene covellite (Fig. 9d). The empirical formula corresponds to $(Ag_{2.90}Au_{0.02})_{\sum 2.92}(Cu_{1.02}Fe_{0.02}Zn_{0.02})_{\sum 1.06}S_{2.02}$. *Mckinstryite* is also scarce and occurs finely disseminated in quartz, associated with cupropolybasite (Fig. 9c) and jalpaite (Fig. 9d). Its average formula is $(Ag_{1.20}Cu_{0.80}Zn_{0.02}Cd_{0.01})_{\sum 2.03}S_{0.97}$, in accord with published compositions of mckinstryite (e.g. Kolitsch 2010; Gamarra-Urrunaga et al. 2013), but in some grains, copper is dominant over silver. This could represent a new mineral species with the average formula $(Cu_{1.54}Ag_{0.46}Zn_{0.01})_{\sum 2.01}S_{0.99}$, which for now is described as Cu-rich mckinstryite (Fig. 9c). It is associated with cupropolybasite and partially replaced by acanthite and silver. Gold-bearing *penzhinite* (?) occurs with chalcopyrite, galena and sphalerite. Its composition approximates $Ag_4(Au,Cu)_2S_3$ which does not match any known mineral, but is closest to penzhinite, $(Ag,Cu)_4Au(S,Se)_4$. It has excess Cu compared with uytenbogaardtite (e.g. Mugas-Lobos et al. 2012; Cocker et al. 2013), and if the formula was calculated according to that mineral, it would give $Ag_{2.77}(Au_{0.83}Cu_{0.61}Fe_{0.08})_{\sum 1.51}S_{1.72}$.

Silver occurs in small irregular grains (up to 10 μm), associated with other Ag-bearing minerals, such as polybasite and cupropolybasite (Fig. 9c), gold and galena. The microprobe analyses give low totals (below 96 wt%) and do not show the presence of other elements, which were sought with EDS, but none were detected. After the analysis, "ablated" pits were observed in the analysis spots so we ascribe the low totals to possible volatilisation of silver under the electron beam.

Supergene minerals

Manganese oxides, formed by variable degrees of supergene replacement of Mn carbonates, dominate supergene alteration (Fig. 7f, g). *Pyrolusite* and *cryptomelane* are the most abundant and occur as big patches (Fig. 9e) or in veinlets, developing botryoidal aggregates with rhythmic banded textures, partly inherited from the primary carbonate from which they have formed. They are associated with minor manganite, manjiroite and wad and locally contain relicts of pyrite, chalcopyrite, sphalerite and galena.

Manjiroite occurs as small patches (Fig. 9e), most of them showing cracked texture, possibly due to gel dehydration. The presence of Na and the absence of K, Ba and Zn were confirmed by EDS indicating an approximate formula (Na)$(Mn^{4+},Mn^{2+})_8O_{16}$.

Lithiophorite —(Al, Li)$Mn^{+4}O_2(OH)_2$—occurs as 10 × 100 μm needles, in radial aggregates (Fig. 9e), locally developing comb textures. Lithiophorite is associated with the other Mn oxide minerals, especially cryptomelane.

Goethite is recurrent and it forms at the expense of pyrite, which it replaces to a variable degree.

Digenite and covellite Digenite and supergene covellite are rare, as partial replacement of chalcopyrite, tennantite-group minerals, cupropearceite, mckinstryite and jalpaite (Fig. 9d).

Philipsburgite —$(Cu,Zn)_6(AsO_4,PO_4)_2(OH)_6{\cdot}H_2O$—was observed at the borders of tennantite, probably replacing it as small grains that are up to 50 μm across (Fig. 9f) which, under the stereoscopic zoom microscope, are light green in colour. The EMP analyses are in reasonable concordance to those given for philipsburgite from the type locality (Peacor et al. 1985), CuO 45.91 (46.3), ZnO 7.53 (18.2), As_2O_5 17.59 (16.3); phosphorus was not analysed. Peacor et al. (1985) presumed that Cu and As were leached from tetrahedrite during weathering reactions, whereas the Zn was leached from sphalerite. The content of ZnO of philipsburgite from Alto de la Blenda is lower than at the type locality, perhaps because the only source of Zn was the tennantite-group minerals, as sphalerite is extremely scarce in the vicinity of philipsburgite.

Fluid inclusion results

Inclusion petrography and microthermometry

The Alto de la Blenda vein contains exclusively small liquid-rich two-phase fluid inclusions (Fig. 10). As in most epithermal deposits, they are abundant but small, generally less than 3 μm especially in the earlier quartz, but we found some between 5 and 20 μm, suitable for microthermometry and LA–ICP–MS studies. Many large fluid inclusions were not usable because they are texturally isolated or, if associated in a fluid inclusion assemblage (FIA), show evidence of necking down (Fig. 10a). The more common shapes are irregular, locally elongated or rounded, and negative crystals. They are two-phase liquid-rich fluid inclusions, and neither daughter crystals nor liquid CO_2 were observed, although some dissolved CO_2 may be present that was not detected as clathrate. Their size, shape and two-phase (liquid-rich) nature are indicative of low temperature trapping conditions (Bodnar et al. 1985). Vapour-rich inclusion assemblages are practically absent.

Representative samples of quartz were selected from each stage of mineralisation. For the last three stages, where an earlier and later quartz generation (a and b) can be differentiated, both were studied. We also analysed a previous quartz (Qp) occurring as phenocrysts in a porphyry clast in the polymictic hanging wall breccia (Fig. 7a). We measured 555 fluid inclusions from 108 assemblages in 32 sections from 19 locations in the Alto de la Blenda vein system (Laboreo, Esperanza and Esperanza SE segments). Table 3 shows the maximum, minimum and average values and the standard deviation of the microthermometry results obtained for each fluid inclusions assemblage, as well as the paragenetic position and the number of fluid inclusions measured in each assemblage.

Quartz 1 (Q1) contains only a few measurable liquid-rich fluid inclusions, which are irregular to elongated and up to 12 μm in size. Some primary inclusions (P) are grouped in isolated clusters or along growth lines (Fig. 10b), whereas the pseudosecondary inclusions (PS) are arranged along fractures inside the crystal. Average salinity and homogenisation temperature are 2.7 wt% NaCl(eq) and 207 ° C; values vary from 2.1 to 3.4 wt% NaCl(eq) and 190 to 219 °C for the Laboreo segment and from 2.1 to 4.3 wt% NaCl(eq) and 171 to 262 °C for the Esperanza segment (see Table 3 for details). Q1 was not recognised in the Esperanza SE segment.

Quartz 2 contains more abundant inclusions than Q1, their size is up to 30 μm, with an average of 13 μm for the ones selected for measurements, and their shape is irregular to elongated for both generations, Q2a and Q2b. Average salinity and homogenisation temperature values are 3.6 (Q2a) to 3.0 (Q2b)

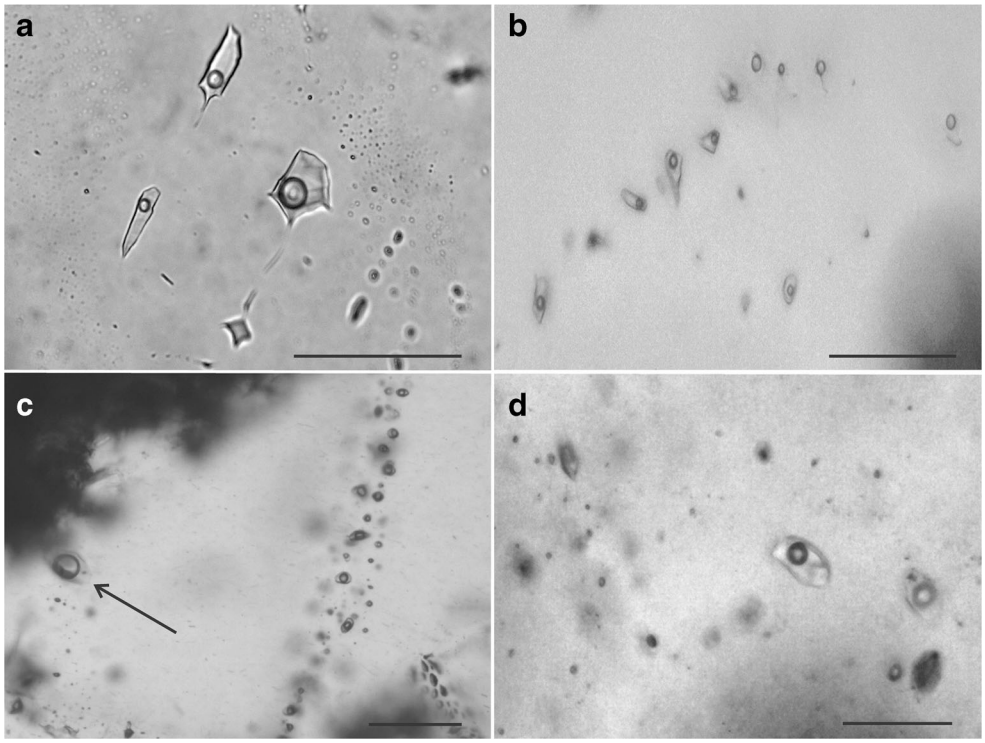

Fig. 10 Photomicrographs of typical fluid inclusion assemblages in successive mineralisation stages. **a** Big fluid inclusions in Q1 show evidence of necking down. **b** Irregular to elongated fluid inclusions along a growth line in Q2b. **c** Intermediate-density fluid inclusions that exclusively occur in quartz fragments of porphyry-type veins or phenocrysts in the polymictic breccia, as trails with consistent vapour to liquid ratios between ~0.4 and 0.6, together with rare individual aqueous-carbonic fluid inclusions with a ratio of total vapour to aqueous liquid around 0.4 and with a thin meniscus of liquid CO_2 (*arrow* to the left of the picture). **d** Three-phase hypersaline brine inclusions (L + V + halite) with high-salinity fluids from a porphyry clast in the polymictic breccia above the Esperanza SE segment, associated with vapour inclusions. *Scale bar* in all photomicrographs is 50 μm

wt% NaCl(eq) and 223 °C (Q2a) to 216 °C (Q2b) (see Table 3 for details).

Quartz 3 (Q3a and Q3b) hosts irregular and elongated fluid inclusions of <3 to 20 μm in average size, with a few tubular inclusions up to 80 μm long and 5 μm wide. Average salinity and homogenisation temperature values are 2.8 (Q3a) to 3.5 (Q3b) wt% NaCl(eq) and 209 °C (Q3a) to 221 °C (Q3b) (see Table 3 for details).

Quartz 4 (Q4a and Q4b) is the latest and the fluid inclusions are also irregular to elongated, and some with negative crystal shapes; the average size of the selected, bigger inclusions used for microthermometry is 25 μm. The average values of salinity and homogenisation temperature are 4.6 (Q4a) to 3.1 (Q4b) wt% NaCl(eq) and 203 °C (Q4a) to 215 °C (Q4b), respectively, and Q4a shows small variations for the Laboreo and Esperanza vein segments (see Table 3 for details). Q4 was not recognised in Esperanza SE segment.

Transparent low-Fe sphalerite of stage 2 from the Esperanza segment (Sp2; Table 3, Fig. 8b) contains fluid inclusions with an average salinity of 2.0 (±0.2) wt% NaCl(eq), which is near the lower end of the salinity range of quartz-hosted inclusions. Homogenisation temperatures averaging 226 (±2) °C are similar to average values obtained in quartz of the same stage of vein mineralisation.

Clasts of the hanging wall breccia (Qp) contain quartz grains with fluid inclusion assemblages that are different from those in all four stages of epithermal vein quartz. We identified three types of fluid inclusion assemblages in these clasts: two-phase liquid-rich fluid inclusions (L + V) with 15–20 vol% vapour and low salinity (Table 3, sample 301-1a, FIA 1); two-phase fluid inclusions (L + V) with low salinity, but exceptionally large vapour bubbles (up to 70 vol%), indicating intermediate density fluids (Fig. 10c, Table 3, sample 301-1a, FIAs 2 and 3), in some inclusions, a thin meniscus of liquid CO_2 was recognised; and three-phase hypersaline fluid inclusions (L + V + halite) (Fig. 10d, Table 3, sample 301-1a, FIA 4). Homogenisation temperatures of the intermediate density and the hypersaline liquid inclusions are well above 300 °C, where heating was stopped to prevent the few available inclusions from decrepitation and allow chemical analysis by LA–ICP–MS.

A fault-hosted vein with sphalerite + galena + quartz from Steve's fault, Bajo de La Alumbrera (BLA; Table 3), shows similar salinity as most of the liquid-rich inclusions in Alto de la Blenda and homogenisation temperatures near the upper

end of the range (3.0 ± 0.1 wt% NaCl(eq) and 261 ± 2 °C in sphalerite; 2.6 ± 0.2 wt% NaCl(eq) and 286 ± 5 °C in quartz).

Figure 11 shows that the highest salinities and homogenisation temperatures tend to occur in the central part of the Alto de la Blenda vein, where the vein is also thickest (Esperanza segment). Figure 11a also shows a temporal trend in the Laboreo segment of the vein, from higher temperatures and lower salinities in the earlier stages 1 and 2 to lower temperatures but higher salinities in the later stages 3 and 4. Despite significant spatial and temporal fluctuations in salinity and temperature, fluid data from all stages of mineralisation in all three segments overlap.

LA–ICP–MS microanalysis

A total of 251 fluid inclusions from 66 assemblages in 23 sections from 16 locations from all segments of the vein system were analysed. Table 4 shows the average concentrations (in μg/g) of the elements Na, S, K, Fe, Cu, As, Ag, Sb, Cs, Au and Pb measured in the fluid inclusions assemblages, as well as the interpreted inclusion origin and the number of fluid inclusions measured in each assemblage. In 14 of those assemblages, only one fluid inclusion was measurable despite petrographic consistency. Element concentrations of the FIAs from the different quartz stages are shown in Fig. 12, and each symbol denotes the average ± 1 standard deviation from one petrographic assemblage of several cogenetic inclusions. Limited values obtained from sphalerite of stage 2 of the Esperanza SE segment (Fig. 12c, orange oval) show that sphalerite-incompatible elements occur in similar concentrations as in quartz-hosted inclusions.

Sodium is invariably the dominant solute, followed by K, Fe and S in similar but variable concentrations. The proportion of K/K + Na tends to decrease from early stage 1 to late stage 4 in each vein segment, i.e. from 0.34 to 0.26 in Laboreo, from 0.44 to 0.31 in Esperanza and from 0.37 to 0.15 in the Esperanza SE segment.

The iron content is higher in the initial stages of the mineralisation, especially in the Laboreo and Esperanza segments, with average values up to 0.64 and 0.96 wt%, respectively. Particularly in the Laboreo segment (Fig. 12a), Fe in the fluids decreases by an order of magnitude from stage 1 to stage 4, with a tendency of increasing overall salinity but falling temperature (Fig. 11a). Sulphur concentrations were detected at high concentration, similar or higher than the most abundant chalcophile metal, iron.

Copper is present in the inclusions in low concentrations, with consistent average values of 0.06 wt% (Laboreo), 0.04 wt% (Esperanza) and 0.02 wt% (Esperanza SE), with a few values of up to 0.4 wt%. Qp also contains low concentrations of this element (0.03 wt% Cu in average; Fig. 12, Table 4). Lead has low average values from less than 0.01 to 0.02 wt%, generally decreasing towards the end of the mineralisation stages. Arsenic and antimony are present in the fluids at concentrations of <0.01 to 0.04 wt%, with the greater values in fluid inclusions of quartz from the stages 2

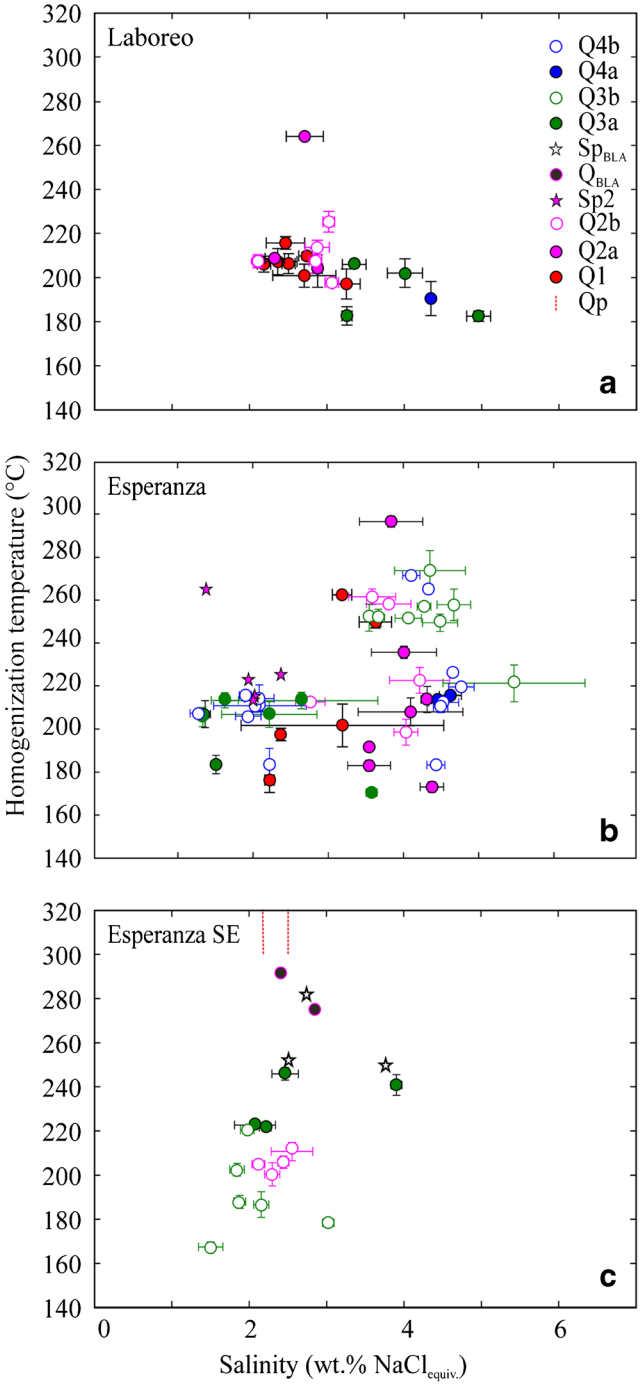

Fig. 11 Th vs. salinity graph showing microthermometry results for the three segments of Alto de la Blenda vein. Higher temperatures to 300 °C are restricted to the central and SE segments hosted by the Alto de la Blenda intrusion, whereas the volcanic-hosted Laboreo segment shows temperatures mostly below 230 °C. These temperatures are minimum trapping temperatures for lack of evidence for coexisting vapour, but the large range in Th requires significant variation in temperature

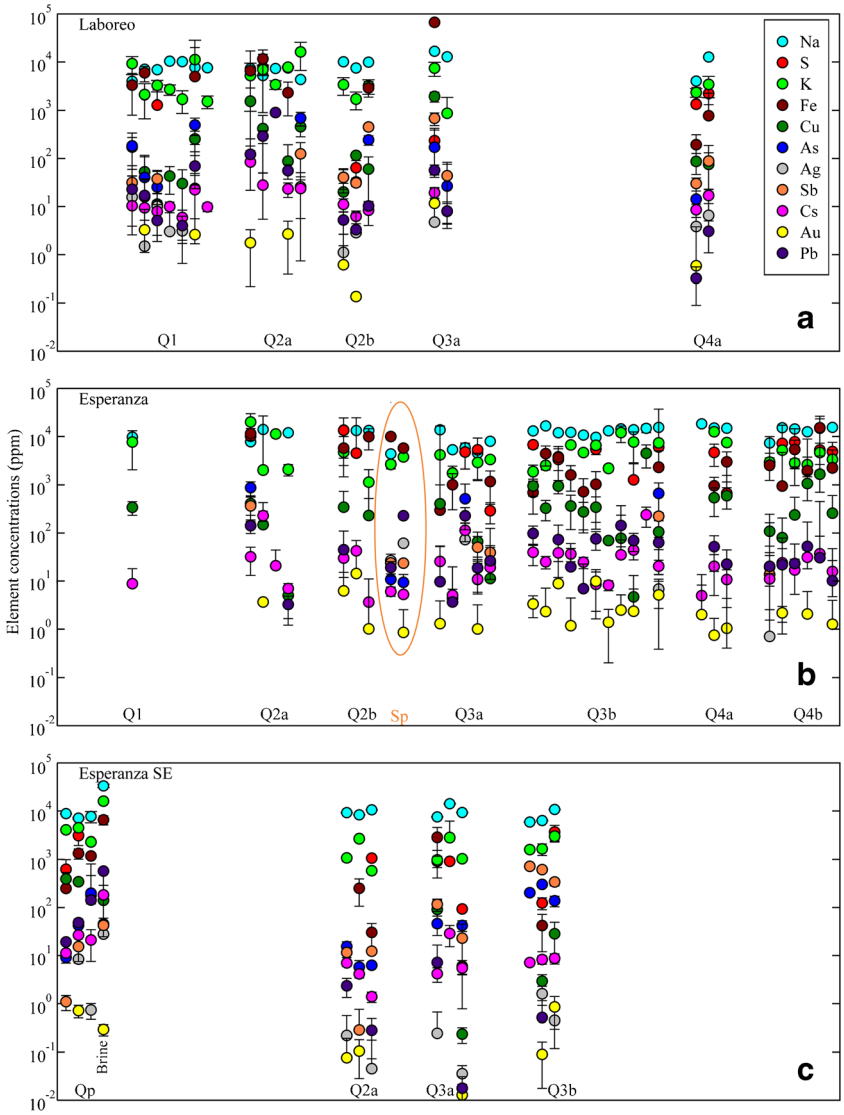

Fig. 12 Element concentrations of fluid inclusions (in ppm by weight, averaged from several inclusions in an assemblage) from the Alto de la Blenda vein, determined by LA-ICPMS. **a**, **b**, **c** Results from each vein segment are sorted according to successive stages of mineralisation. The *orange oval* marks data from sphalerite-hosted inclusions

and 3, where sulphosalts are part of the vein assemblage. Silver was detected in Q2 and Q3, with concentrations up to 15 ppm and an isolated value of 41 ppm for Q3 from the Esperanza segment.

Gold was detected in many fluid inclusions of all stages, thanks to an extended dwell time covering about 40 % of the measurement cycle. For each inclusion, analysed with the protocol for Au analysis (see Sampling and analytical methods), the detection limit for gold was calculated, and all data from each assemblage were sorted in order of decreasing detection limit, as shown in Fig. 13a–c; Fig. 13d–f shows the detected concentrations of Au as a function of the fluid inclusion size. Every Au peak represented by a point in Fig. 13a, b or c was carefully verified to be a clearly detected signal according to the statistical criterion of Pettke et al. (2012), and temporally matching the highest peak of major elements released from the inclusion. The possibility of surface contamination can be excluded, because the samples were carefully and repeatedly cleaned in aqua regia and numerous blank measurements showed a clean sample surface without Au peaks. Gold values ranging from 0.2 to 20 ppm and some as high as 80 ppm all represent significant individual values for gold that is indeed contained in single inclusions. However, Fig. 13a–c also shows that most of the highest calculated gold concentrations are associated with the highest calculated detection limits, which represent the weakest Na signals because concentrations are referenced to Na as internal standard. These high values, although clearly detected gold in the inclusion, are therefore the least reliable fluid analyses and represent, most likely, accidentally trapped nanoparticles of gold. By contrast, many assemblages, such as the green Q3b assemblages in Fig. 13b, yielded more consistent but lower gold concentrations of ~0.5–3 ppm in inclusions with the lowest LODs, which correspond to the best inclusion signals

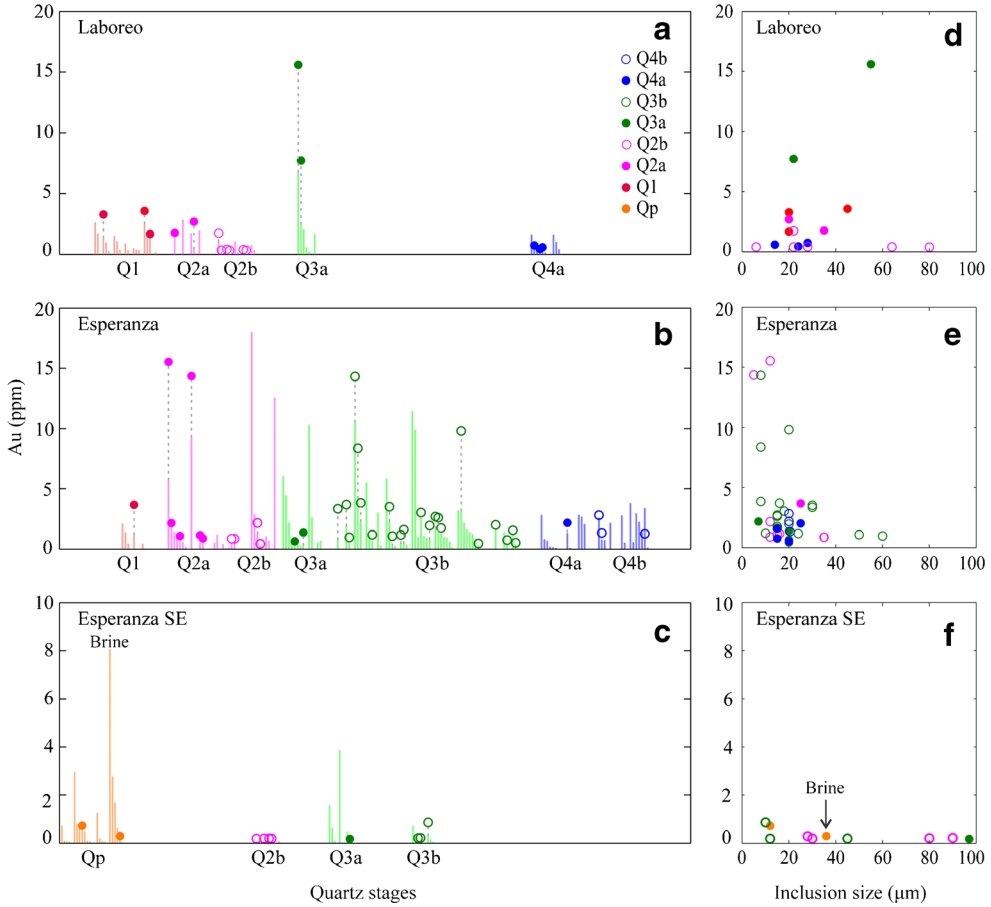

Fig. 13 **a**, **b**, **c** LA–ICP–MS results for Au (in ppm) from individual fluid inclusions in the Laboreo, Esperanza and Esperanza SE segments. Plots in *left column* show single-inclusion gold data with detected values (*circles* for fluid inclusions in quartz, *stars* in sphalerite) as well as detection limits (*bars*), grouped by assemblages and mineralisation stage, and in each assemblage sorted in order of decreasing calculated detection limit. **d**, **e**, **f** The detected concentrations as function of inclusion size. See text for the discussion

with high Na peaks. These systematics suggest that the total variation in analysed gold content is not merely due to a statistical sampling bias in a homogeneous data population of small count numbers, as discussed in Rauchenstein-Martinek et al. (2014). Rather, the data set includes assemblages in which gold at ~0.5–3 ppm was detected and correctly quantified as representing true fluid concentrations (e.g. assemblages Q2b and Q4a in Fig. 13a, several assemblages in Q3a and Q4a and Q4b in Fig. 13b and assemblages Q2a and Q3b in Fig. 13c). These subsets for likely dissolved gold concentration were averaged and are reported in Table 4 and Fig. 12.

Element variation diagrams (Fig. 14) emphasise the small total variation in salinity and in the dominant cation element, Na, compared to that of other metals. The variation of Cs as one of the least reactive and most fluid-conservative elements (Fig. 14a) is small and essentially random. The variation in K (Fig. 14b) is somewhat larger, with the highest values of K/Na ~1 in deep porphyry clast-hosted fluids (QP, Q1, Q2a) decreasing to ~0.1 in some of the later fluid of each stage (the "b" substages) albeit with large random scatter due to the high analytical background on K. Lead shows the greatest variations (Fig. 14c), with the highest Pb/Na ratios in some early inclusion assemblages of the main mineralisation stages (notably some of Q2a) decreasing over more than 2 orders of magnitude to some of the post-ore quartz precipitation substages (barren quartz Q2b, Q3b and Q4b).

Figure 15 illustrates, on a set of three-component plots, that the low-salinity fluids of Alto de la Blenda are relatively Pb poor but rich in As and Sb, which stands in contrast to inclusions of high-salinity magmatic brines in porphyry deposits that tend to be rich in base metals including Pb, Zn and Cu. The only Pb-enriched point is a brine inclusion assemblage from a porphyry clast in the polymictic breccia (Qp from Esperanza SE).

Discussion

Farallón Negro–Alto de la Blenda is a typical carbonate–base metal–gold deposit in the sense of Corbett and Leach (1998)

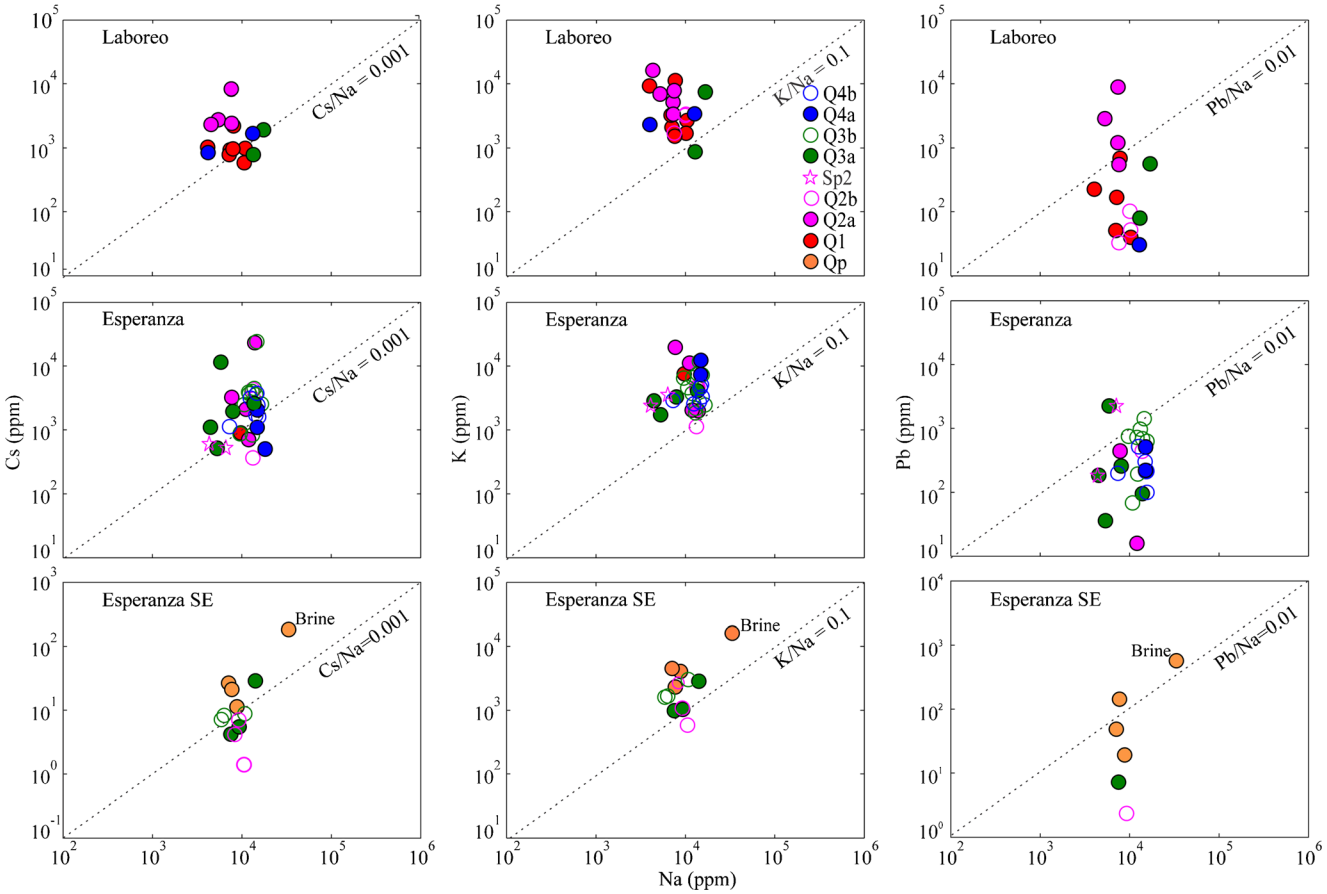

Fig. 14 LA–ICP–MS measurements of concentrations of **a** Cs (*left*), **b** K (*centre*) and **c** Pb (*right*) plotted against Na concentrations, separated into rows for each segment of the Alto de la Blenda vein. *Symbols* represent the average value of several inclusions in one fluid inclusion assemblage; *circles* represent fluid inclusions in quartz, *stars* in sphalerite; *filled symbols* denote the earlier "a" substages and *empty symbols* denote the barren "b" substages of each stage represented by *colours*. *Qp* are inclusion assemblages in porphyry clasts of the polymictic breccia. The *45° lines* correspond to constant element proportions

or an intermediate-sulphidation epithermal gold deposit as defined by Hedenquist et al. (2000) and Sillitoe and Hedenquist (2003). Such deposits are generally associated with intermediate composition calc-alkaline hydrous magmas reaching the upper crust. Their general geology and common association with porphyry copper deposits (Sillitoe 2010) suggests an ore-forming process that includes at least a partial input of magmatic fluids (Heinrich 2005; Sillitoe 2010). A stable-isotope analysis of a low-salinity (0.4 wt% NaCl(eq)) fluid inclusion extract from a quartz–rhodochrosite vein of Alto de la Blenda yielded a $\delta D = 70$ permil identical to magmatic fluids extracted from quartz-magnetite alteration and a $\delta^{18}O$ value of 0 permil, which is about half-way between the magmatic range and the meteoric water line (Ulrich et al. 2002). These data and the minor shift of $\delta^{18}O$ of fluids associated with feldspar-destructive alteration at Bajo de la Alumbrera could be explained by mixing of low-salinity magmatic fluid with isotopically lighter meteoric water (Ulrich et al. 2002), but more likely reflects interaction of dominantly magmatic fluids with igneous wall rocks at epithermal temperatures (Harris et al. 2005). The extensive breccia zone along the hanging wall of the Alto de la Blenda vein has the

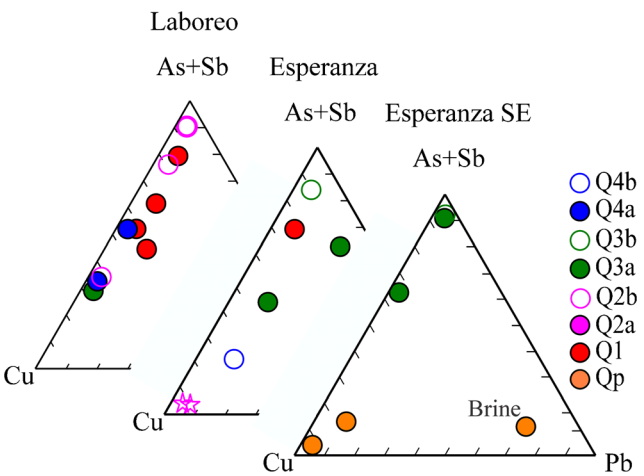

Fig. 15 LA–ICP–MS data showing the proportions of Cu, As + Sb and Pb, plotted in a *triangular* diagram, for each of the vein segments. *Symbols* and *colours* are the same as used in Figs. 13 and 14

textural characteristics of a large pebble dyke, including a polymictic mixture of rounded fragments in a sandy matrix, indicating forceful and turbulent emplacement driven by expanding magmatic fluids. It contains fragments of quartz–feldspar porphyry that host high-temperature intermediate-density fluid inclusions, which resemble inclusion assemblages in the roots of deep-seated porphyry deposits (e.g. Rusk et al. 2008; Landtwing et al. 2010). Their association with fragments of basement granite indicates fluid-driven mechanical transport from greater depth. The breccia contains fragments of sphalerite, demonstrating emplacement after the first epithermal veins were formed, but it is also cut by later stage rhodochrosite–base metal–gold veins (Fig. 7), and is therefore temporally associated with the formation of the deposit. The poorly exposed and un-dated quartz–feldspar porphyry intrusion at the northeastern end of the deposit (Fig. 3) is cut by epithermal rhodochrosite veins with little or no gold and base metals (Fig. 4d), resembling the latest stage of the Alto de la Blenda veins (Fig. 7e).

The paragenetic sequence of the Alto de la Blenda deposit allows a tentative correlation of the four stages of mineralisation in three segments of the vein system, indicating major pulses of fluid injection and mineral precipitation affecting the entire vein. The vein mineralogy is dominated by quartz and carbonates (>90 % by volume), plus pyrite as the most widely distributed sulphide mineral. Pyrite is As-poor but repeatedly showed significant Au contents, indicating that some of the gold is refractory and enclosed in pyrite as nanoparticles, but not in solid solution as in many sediment-hosted epithermal gold deposits (Reich et al. 2005; Deditius et al. 2011). Base metal and partly precious metal-bearing sulphides, sulphosalts, tellurides and native gold precipitated mainly in the second and third stage of mineralisation, separated by barren Mn-rich carbonates and granular to vuggy quartz. Stage 4 hydrothermal event still contains minor sphalerite and chalcopyrite, but negligible precious metals. No mine-scale data on gold distribution are available, but Alto de la Blenda appears to lack any vein portions with bonanza-grade gold concentrations. This contrasts with otherwise comparable carbonate–base metal–gold deposits like Porgera (Papua New Guinea; Richards et al. 1997), Roşia Montană (Romania; Wallier et al. 2006) or the thin but very high-grade veins of Buriticá (Colombia; Lesage et al. 2013).

Fluid inclusion assemblages associated with successive vein stages at Alto de la Blenda indicate significant fluctuations in temperature, salinity and elemental composition. They show little or no evidence of fluid boiling in the vein, such as vapour-rich inclusions or inclusion assemblages with variable liquid/vapour proportions. Their absence is consistent with a lack of mineralogical indicators for boiling, such as vein adularia (Browne and Ellis 1970) or bladed calcite (Keith and Muffler 1978). Homogenisation temperatures range from 167 ± 2 to 295 ± 3 °C with small variations within assemblages, but show no systematic relation to depth in the mine as observed in boiling geothermal systems (e.g. Hedenquist et al. 1992). This range is too large to be explained by variable pressure correction within the single-phase liquid field and provides clear indications of repeated hotter fluid pulses followed by cooling to lower temperatures (e.g. Fig. 11c). Fluid salinity also varies significantly, but within a small range of 2 to 4 wt% NaCl(eq) for most assemblages and with very consistent values in each assemblage. This variation could represent ~50 % dilution of a moderately saline (4 %) magmatic fluid by low-salinity meteoric water or salt enrichment by limited boiling of an initial fluid at the low-salinity end of the spectrum, for which there is no evidence. More likely, therefore, the small salinity variation reflects processes in the source region of these fluids—either primary salinity variation due to selective partitioning of Cl and H_2O from melt to fluid, or minor brine separation in a subjacent porphyry domain (Cline and Bodnar 1991; Heinrich and Candela 2014). Fluids of similarly low salinity (2.5 %) but lower density (Fig. 10c) occur in porphyry fragments of the inter-mineral polymictic breccia, indicating the presence of hotter fluids of similar composition below the deposit before or during epithermal vein mineralisation. Textural evidence and inclusion sizes are inadequate to ascertain whether these low-density fluids coexisted as a vapour phase with the rare brine inclusions occurring in the same samples (Fig. 10d), or whether they represent a single-phase ('supercritical') magmatic fluid.

LA–ICP–MS analyses indicate variably enriched concentrations of heavy alkali metals (K, Cs), base metals including Pb and Cu, and particularly of S, As, Sb, Ag and Au in the epithermal ore fluids. Metal concentrations are notably higher than in fluids from active arc-related geothermal systems on land (e.g. Einaudi et al. 2003; Simmons and Brown 2007; Simpson et al. 2015). They are more comparable to low-salinity magmatic-hydrothermal vapour inclusions of low to intermediate density occurring in porphyry ore systems (Audétat et al. 1998; Audétat et al. 2008; Kouzmanov and Pokrovski 2012) including the vapour phase in the Bajo de la Alumbrera Cu–Au porphyry (Ulrich et al. 2002). Vein fluids are somewhat lower-salinity and cooler compared with in late carbonate–base metal–gold veins cutting the Alumbrera porphyry–Cu–Au ore (Fig. 11c). They are more similar to low-salinity ore fluids that formed the breccia-hosted gold deposit of Roşia Montană (Romania), where constant O–H isotope composition despite variable temperature shows a dominantly magmatic source (Wallier et al. 2006). Qp clasts include higher-temperature inclusions of similar 2–4 % salinity and overlapping elemental composition. Based on their high content of As, Sb and S, we interpret the 2–4 wt% NaCl(eq) inclusions as a dominantly magmatic fluid that was derived by cooling and

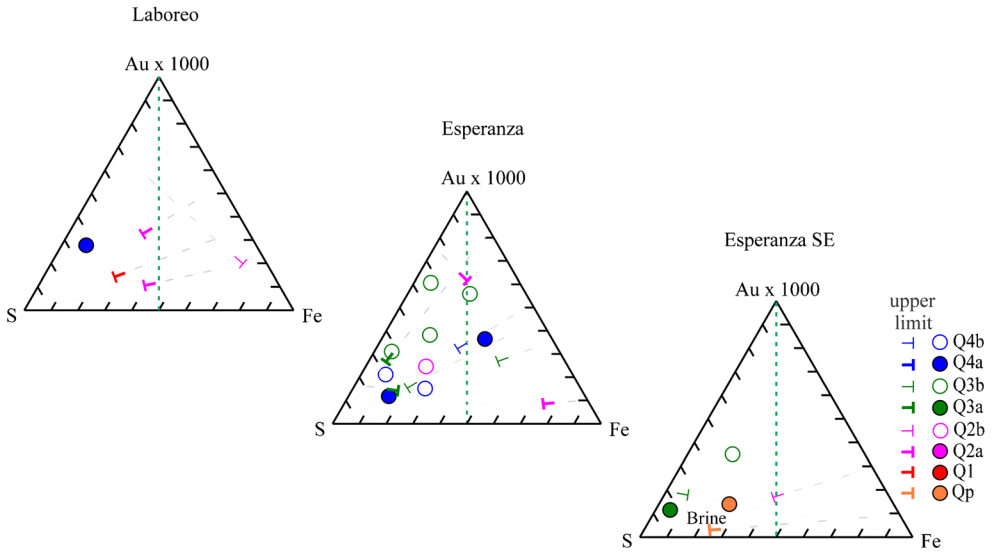

Fig. 16 LA–ICP–MS data of individual fluid inclusions showing the proportions of S, Au (×1000) and Fe in triangular diagrams, for all assemblages where concentrations of 0.5–3 ppm Au were considered significant and representative of a homogeneous ore fluid, following critical assessment of limits of detection (see text and Fig. 13). Where one of the elements, S or Fe, was below the limit of detection, its upper concentration limit is indicated by the *cross-bar* of the corresponding T symbols. The *green line* marks the concentration ratio S:Fe = 1:1, showing that nearly all Au-rich fluids contain S in excess of Fe, or may contain S excess based on the respective limits of detection

contraction of magmatic vapour. This vapour probably condensed out some brine at depth, represented by the one assemblage with 35 wt% NaCl(eq). recorded by a porphyry clast in the polymictic breccia, which is enriched in Pb, Fe and Cs but depleted in As and Sb (Table 4, assemblage 301–12-FIA4; "brine" labelled circles in Figs. 12, 13, 14, 15 and 16). Initially, high K/Na and Fe/Na trending towards lower values in later stages are consistent with a magmatic fluid experiencing variable degrees of modification by wall rock alteration to sericite and pyrite.

Gold analyses (Fig. 13) have yielded the first evidence for high gold concentrations in an epithermal ore fluid, in the range of 0.5 to 3 ppm. These concentrations are 1–2 orders of magnitude higher than those in any active geothermal fluids (Brown 1986; Simmons and Brown 2006, 2007; cf. Heinrich 2006), but match the high gold concentrations found in porphyry-mineralizing magmatic vapour inclusions (Ulrich et al. 1999), which were used as a basis for thermodynamic modelling of gold transport across the porphyry-to-epithermal transition (Heinrich et al. 2004; Heinrich 2005). In contrast to high copper contents of magmatic vapour inclusions (which are now recognised as product of post-entrapment modification; Lerchbaumer and Audétat 2012), preferential gold transport in sulphur-rich magmatic vapour has been confirmed experimentally (Pokrovski et al. 2008), and the high gold concentrations observed in porphyry-related vapour inclusions are unlikely to be artefacts of post-entrapment modification (Seo and Heinrich 2013). Epithermal fluid inclusions with ~1 ppm Au reported here are consistent with calculated gold solubility at epithermal temperatures, provided that the fluids are mildly oxidised and sulphur rich (sulphate ~ H_2S) and do not contain a large excess of Fe relative to sulphide. Even though our analyses of S, Fe and Au are subject to large analytical uncertainty, nearly all inclusion assemblages with reliably high Au concentrations contain S > Fe on a weight basis, or at least a twofold excess of S compared to Fe on a molar basis (plotting on the left side of the dashed green line in Fig. 16). These results confirm the thermodynamic prediction that contracted magmatic vapour with excess sulphide over chalcophile metals is the most effective ore fluid for epithermal gold mineralisation (Heinrich et al. 2004; Heinrich 2005).

The deposition of gold at Alto de la Blenda was probably driven by the precipitation of pyrite and base metal sulphides, which led to the removal of sulphur from the fluid and thus reduced gold solubility as $Au(HS)^{2-}$ (with quadratic effect due to the ligand number 2 in the gold bisulphide complex; Stefánsson and Seward 2004). De-sulphidation of a contracted magmatic vapour initially containing a small excess of reduced sulphur compared with chalcophile metals (Fe, Zn, etc.) can explain the relatively modest but persistent gold grades in the carbonate–base metal–gold veins of Alto de la Blenda. This rather quiescent mechanism of gold precipitation from a cooling single-phase epithermal liquid may be an essential difference between Alto de la Blenda and more spectacular deposits like Porgera, Buriticá or Roşia Montană, where flash boiling (e.g. Simpson et al. 2015) and/or reduction by carbonaceous host rocks led to locally very high gold grades.

Summary and conclusions

(1) Farallon Negro–Alto de la Blenda is a large carbonate–base metal–gold vein system of intermediate-sulphidation type, showing repeated vein opening, forceful brecciation and injection of igneous material from greater depth, which demonstrate hydrothermal ore formation in a magmatically active subvolcanic environment close to a slightly older world-class porphyry Cu–Au deposit.

(2) The vein mineralogy is quartz–carbonate dominated with minor sulphides and shows a consistent paragenetic sequence with multiple stages of mineralisation that can be correlated over the kilometre extent of the Alto de la Blenda vein system.

(3) Hydrothermal fluid temperature fluctuated significantly during mineralisation (160–300 °C) but fluid salinity was confined to a narrow range (~2–4 wt%), and neither fluid inclusions evidence nor mineral textures indicate significant boiling during ore formation. Salinity and major and trace element concentrations of the mineralising fluids are orders of magnitude higher than in active geothermal fluids dominated by convecting groundwater. They indicate, consistent with limited stable isotope data, derivation of the epithermal liquids and their solutes by cooling and contraction of a magmatic vapour.

(4) A new approach to assess analytical detection limits of gold in fluid inclusion assemblages demonstrates that the fluids were rich in S and contained Au at the parts per million level, with S in excess over Fe and base metals. Such fluid–chemical characteristics are optimal for gold transport from their magmatic source, to generate a high-grade gold deposit.

(5) Our results imply that fluid characteristics as well as the large spatial extent of the magmatic-hydrothermal systems would have been suitable to generate a much richer deposit of world-class quality. Most likely, geological ingredients allowing sharp gradients in gold solubility (e.g. flash boiling or chemical reductants) were missing to precipitate higher-grade ores. On the positive side, this inference implies good prospectivity for other (e.g. shallower) epithermal deposits in the region and good chances for continuity of similar ore grades beneath the Alto de la Blenda mine.

Acknowledgments This study was supported by CONICET of Argentina through a PIP 112-20120100554-CO grant. Field and analytical parts of this study were supported by the Swiss National Science Foundation grant 200020_135302. The authors are grateful to P. černý for the microprobe access at the University of Manitoba; to M. Guillong and M. Wälle for their help obtaining the LA-ICP-MS data at ETH Zurich; to D. Meier for introducing MFMZ to the SILLS program; to Minera Alumbrera SA for their financial support and accomodation during the field trips to the FNVC and to the staff at YMAD and especially to the chief geologist, N. Montenegro, for their help during geological mapping and sampling at the Farallón Negro mine. The authors are very grateful for the constructive reviews of T. Ulrich and J. L. Mauk; the editorial handling of Associate Editor Dave Craw and the editorial comments of G. Beaudoin and are much appreciated.

References

Alderete MC (1999) Distrito Farallón Negro-Alto de la Blenda, Catamarca. In: Zappettini EO (ed) Recursos Minerales de la República Argentina, SEGEMAR, Anales 35, Buenos Aires, pp 1637–1642

Allison AE (1986) The geology of the Bajo El Durazno porphyry copper-gold prospect, Catamarca Province, Argentina. M.Sc. Dissertation, University of Arizona

Allmendinger RW (1986) Tectonic development, southeastern border of the Puna plateau. Geol Soc Am Bull 97:1070–1082

Allmendinger RW, Ramos VA, Jordan TE, Palma M, Isacks BL (1983) Paleogeography and Andean structural geometry, northwest Argentina. Tectonics 2:1–16

Angelelli V (1984) Yacimientos Metalíferos de la República Argentina II. Comisión de Investigaciones Científicas, Buenos Aires, pp 401–402

Angera JA (1999) Mina Bajo de la Alumbrera, Catamarca. In Zapettini EO (ed) Recursos Minerales de la República Argentina, SEGEMAR, Anales 35, Buenos Aires, pp 1451–1461

Armstrong JT (1993) Caltech 1993 JEOL license of CITZAF version 3.5

Audétat A, Günther D, Heinrich CA (1998) Formation of a magmatic hydrothermal ore deposit; insights in with LA-ICP-MS analysis of fluid inclusions. Science 279:2091–2094

Audétat A, Pettke T, Heinrich CA, Bodnar RJ (2008) The composition of magmatic-hydrothermal fluids in barren and mineralized intrusions. Econ Geol 103:877–908

Barazangi M, Isacks B (1976) Spatial distribution of earthquakes and subduction of the Nazca plate beneath South America. Geology 4: 686–692

Bevis M, Isacks B (1984) Hypocentral trend surface analysis: probing the geometry of the Benioff zones. J Geophys Res 89:6153–6170

Bodnar RJ, Vityk, MO (1994) Interpretation of microthermometric data for NaCl-H2O fluid inclusions. In: De Vovo B, Frenzzotti, ML (eds) Fluid inclusions in minerals: methods and applications. Short course of the working group (IMA) "Inclusions in Minerals", Blacksburg, VA, USA, pp. 117/131

Bodnar RJ, Reynolds TJ, Kuehn CA (1985) Fluid-inclusion systematics in epithermal systems. Rev Econ Geol 2:73–97

Breitenmoser T (1999) Geology and geochemistry of the calc-alkaline Farallón Negro Volcanic Complex at Capillitas, NW-Argentina. MSc Thesis, ETH Zürich. 77 pp, 1 map

Brown KL (1986) Gold deposition from geothermal discharges in New Zealand. Econ Geol 81:979–983

Brown S (2004) Geología y mineralización del yacimiento de cobre-oro de Bajo de la Alumbrera. In: Márquez-Zavalía MF (ed) Curso Latinoamericano de Metalogenia UNESCO-SEG. Guía de campo, Mendoza, pp 101–120

Browne PRL, Ellis AJ (1970) Ohaki-Broadlands hydrothermal area, New Zealand—mineralogy and related geochemistry. Am J Sci 269:97–131

Cahill T, Isacks B (1992) Seismicity and shape of the subducted Nazca plate. J Geophys Res 97:17503–17529

Cline JS, Bodnar RJ (1991) Can economic porphyry copper mineralization be generated by a typical calc-alkaline melt? J Geophys Res 96: 8113–8126

Cocker H, Mauk J, Rabone SC (2013) The origin of Ag–Au–S–Se minerals in adularia-sericite epithermal deposits: constraints from the Broken Hills deposit, Hauraki Goldfield, New Zealand. Mineral Deposita 48:249–266

Corbett GJ, Leach TM (1998) Southwest Pacific rim gold-copper systems: structure, alteration, and mineralisation. Soc Econ Geol Spec Pub 6. 234 pp

Coughlin TJ, O'Sullivan PB, Kohn BP, Holcombe RJ (1998) Apatite fission-track thermochronology of the Sierras Pampeanas, central western Argentina: implications for the mechanism of plateau uplift in the Andes. Geology 26(11):999–1002

Deditius AP, Utsunomiya S, Reich M, Kesler SE, Ewing RC, Hough R, Walshe J (2011) Trace metal nanoparticles in pyrite. Ore Geol Rev 42(1):32–46

Einaudi MT, Hedenquist JW, Inan EE (2003) Sulfidation state of fluids in active and extinct hydrothermal systems: transitions from porphyry to epithermal environments. In: Simmons ST (ed) Volcanic, geothermal and ore-forming fluids. Soc Econ Geol Spc Pub 10, pp 304–321

Fielding EJ, Jordan TE (1988) Active deformation at the boundary between the Precordillera and Sierras Pampeanas, Argentina and comparison with ancient Rocky Mountain deformation. Geol Soc Am 171:143–163

Franchini M, Impiccini A, Oleary S, Ríos FJ, Schalamuk IB (2009) Distribución de las alteraciones y mineralizaciones en la sección central del yacimiento Agua Rica (27°22'S-66°16'O), Catamarca. Rev Asoc Geol Argent 64:391–408

Franchini M, Impiccini A, Lentz D, Ríos FJ, Oleary S, Pons J, Schalamuk IB (2011) Porphyry to epithermal transition in the Agua Rica polymetallic deposit, Catamarca, Argentina: an integrated petrologic analysis of ore and alteration parageneses. Ore Geol Rev 41:49–74

Franchini M, McFarlane C, Maydagán L, Reich M, Lentz DR, Meinert L, Bouhier V (2015) Trace metals in pyrite and marcasite from the Agua Rica porphyry-high sulfidation epithermal deposit, Catamarca, Argentina: textural features and metal zoning at the porphyry to epithermal transition. Ore Geol Rev 66:366–387

Gamarra-Urrunaga JE, Castroviejo R, Bernhardt H-J (2013) Preliminary mineralogy and ore petrology of the intermediate-sulfidation Pallancata deposit, Ayacucho, Peru. Can Mineral 51:67–91

Gimeno Torrente D, Carrazana A, Bruna Novillo J, Fernández Turiel JL (2011) Mineralogía del Prospecto Bajo Agua Tapada, Catamarca, Argentina. Macla 15:99–100

Godeas M, Segal S (1980) Alteración hidrotermal y mineralización en el Bajo de la Alumbrera, provincia de Catamarca. Rev Asoc Geol Argent 35:318–331

Goldstein RH, Reynolds TJ (1994) Systematics of fluid inclusions in diagenetic minerals. Soc Sediment Geol, Short Course 31, Tulsa, OK, USA

González OE (1975) Geología y alteración en el cobre porfídico "Bajo la Alumbrera", República Argentina. II Congr Ibero-Am Geol Econ, Buenos Aires, pp 247–270

González Bonorino F (1950a) Algunos problemas geológicos de las Sierras Pampeanas. Rev Asoc Geol Argent 5:81–110

González Bonorino F (1950b) Geología y petrología de las hojas 12-D (Capillitas) y 13-D (Andalgalá): Dirección General de Industria y Minería, Bol 70, Buenos Aires. 92 pp

Guilbert JM (1995) Geology, alteration, mineralization, and genesis of the Bajo de la Alumbrera porphyry copper-gold deposit, Catamarca province, Argentina. Ariz Geol Soc Dig 20:646–656

Guillong M, Latkoczy C, Seo JH, Günther D, Heinrich CA (2008) Determination of sulfur in fluid inclusions by laser ablation ICP-MS. J Anal At Spectrom 23:1581–1589

Günther D, Audetat A, Frischknecht R, Heinrich CA (1998) Quantitative analysis of major, minor and trace elements in fluid inclusions using laser ablation inductively coupled plasma mass spectrometry. J Anal At Spectrom 13(4):263–270

Halter WE, Bain N, Becker K, Heinrich CA, Landtwing MR, Von Quadt A, Clark AH, Sasso AM, Bissig T, Tosdal RM (2004) From andesitic volcanism to the formation of a porphyry Cu-Au mineralizing magma chamber: the Farallón Negro Volcanic Complex, northwestern Argentina. J Volcanol Geotherm Res 136:1–30

Halter WE, Heinrich CA, Pettke T (2005) Magma evolution and the formation of porphyry Cu-Au ore fluids; evidence from silicate and sulphide melt inclusions. Mineral Deposita 39:845–863

Harris AC, Kamenetsky VS, White NC, van Achterbergh E, Ryan CG (2003) Melt inclusions in veins: linking magmas and porphyry Cu deposits. Science 302:2109–2111

Harris AC, Golding SD, White NC (2005) Bajo de la Alumbrera copper-gold deposit: stable isotope evidence for a porphyry-related hydrothermal system dominated by magmatic aqueous fluids. Econ Geol 100:863–886

Harris AC, Bryan SE, Holcombe RJ (2006) Volcanic setting of the Bajo de la Alumbrera porphyry Cu-Au deposit, Farallon Negro Volcanics, Northwest Argentina. Econ Geol 101:71–94

Hedenquist JW, Henley RW (1985) The importance of CO_2 on freezing-point measurements of fluid inclusions—evidence from active geothermal systems and implications for epithermal ore deposition. Econ Geol 80:1379–1406

Hedenquist JW, Reyes AG, Simmons SF, Taguchi S (1992) The thermal and geochemical structure of geothermal and epithermal systems—a framework for interpreting fluid inclusion data. Eur J Mineral 4: 989–1015

Hedenquist JW, Arribas A Jr, Gonzalez-Urien E (2000) Exploration for epithermal gold deposits. Rev Econ Geol 13:245–277

Heinrich CA (2005) The physical and chemical evolution of low-salinity magmatic fluids at the porphyry to epithermal transition: a thermodynamic study. Mineral Deposita 39:864–889

Heinrich CA (2006) How fast does gold trickle out of volcanoes? Science 314:263–264

Heinrich CA, Candela PA (2014) Fluids and ore formation in the Earth's crust: treatise on Geochemistry, ed. 2:13, pp 1–28

Heinrich CA, Pettke T, Halter WE, Aigner-Torres M, Audetat A, Günther D, Hattendorf B, Bleiner D, Guillong M, Horn I (2003) Quantitative multi-element analysis of minerals, fluid and melt inclusions by laser-ablation inductively-coupled plasma mass-spectrometry. Geochim Cosmochim Acta 67:3473–3497

Heinrich CA, Driesner T, Stefánsson A, Seward TM (2004) Magmatic vapor contraction and the transport of gold from the porphyry environment to epithermal ore deposits. Geology 32:761–764

Heinrich CA, Halter W, Landtwing MR, Pettke T (2005) The formation of economic porphyry copper (-gold) deposits: constraints from microanalysis of fluid and melt inclusions. Geol Soc Lond, Sp Publ 248, Fermor Vol, pp 247–263

Heinrich CA, Meier D, Erni M, von Quadt A, Márquez-Zavalía MF (2011) Life-times and scales of Cu-Au-mineralizing magmatic-hydrothermal processes: Farallón Negro (Argentina). 11th Bienn SGA Meeting, Antofagasta, pp 3–6

Hug A (1999) Petrography and genesis of the Capillitas diatreme, Farallón Negro Volcanic Complex, NW-Argentina. MSc Thesis, ETH Zürich. 74 pp

JICA (Japan International Cooperation Agency) (1978–81) Informe de estudios básicos sobre la explotación de recursos minerales en la zona norte de la República Argentina (1978–81). Cuatro etapas. Dir Gen Fabr Mil, Unpublished report, Buenos Aires

JICA (Japan International Cooperation Agency) (1986–89) Informe sobre Exploración Exploración Minera en la Zona de Alto de la Blenda, República Argentina. Fase I. YMAD, Catamarca, Unpublished report

Isacks B, Jordan T, Almendinger R, Ramos VA (1982) La segmentación tectónica de los Andes Centrales y su relación con la placa de Nazca subductada: V Congreso Latinoamericano de Geología, Actas III. Buenos Aires, pp 587–606

Jones JP (1994) The Farallón Negro Bajo de la Alumbrera volcano-plutonic cluster. 7 Cong Geol Chileno 2:1571–1575

Jones JP (1996) The Farallón Negro-Bajo de la Alumbrera volcano-plutonic cluster. 13 Cong Geol Argentino 3:17–27

Jordan TE, Allmendinger RW (1986) The sierra pampeanas of Argentina: a modern analog of Rocky Mountain foreland deformation. Am J Sci 286:737–764

Jordan TE, Bryan LI, Allmendinger RW, Brewer JA, Ramos VA, Ando CJ (1983) Andean tectonics related to geometry of subducted Nazca plate. Geol Soc Am Bull 94:341–361

Kay S, Mpodozis C, Coira B (1999) Neogene magmatism, tectonism, and mineral deposition of the Central Andes (22° to 33° S latitude). Soc Econ Geol Spec Publ 7:27–59

Keith TEC, Muffler LJP (1978) Minerals produced during cooling and hydrothermal alteration of ash flow tuffs from Yellowstone Drill Hole Y-5. J Volcanol Geotherm Res 3:373–402

Kolitsch U (2010) The crystal structure and compositional range of mckinstryite. Mineral Mag 74:73–84

Koukharsky M, Mirré JC (1976) Mi Vida prospect: a porphyry copper type deposit in northwestern Argentina. Econ Geol 71:849–863

Kouzmanov K, Pokrovski GS (2012) Hydrothermal control on metal distribution in porphyry Cu (-Mo-Au) systems. SEG Spec Pub 16: 573–618

Landtwing MR, Dillenbeck ED, Leake MH, Heinrich CA (2002) Evolution of the breccia-hosted porphyry Cu-Mo-Au deposit at Agua Rica, Argentina: progressive unroofing of a magmatic hydrothermal system. Econ Geol 97:1273–1292

Landtwing MR, Furrer C, Redmond PB, Pettke T, Guillong M, Heinrich CA (2010) The Bingham Canyon porphyry Cu-Mo-Au deposit. III. Zoned copper-gold ore deposition by magmatic vapor expansion. Econ Geol 105:91–118

Lerchbaumer L, Audétat A (2012) High Cu concentrations in vapor-type fluid inclusions: an artifact? Geochim Cosmochim Acta 88:255–274

Lesage G, Richards JP, Muehlenbachs K, Spell TL (2013) Geochronology, geochemistry, and fluid characterization of the late Miocene Buriticá gold deposit, Antioquia Department, Colombia. Econ Geol 108:1067–1097

Linares E, González RA (1990) Catálogo de edades radimétricas de la República Argentina 1957–1987. Pub Especial Rev Asoc Geol Arg Serie B, 19

Llambías EJ (1970) Geología de los Yacimientos Mineros Agua de Dionisio, Provincia de Catamarca, República Argentina. Rev Asoc Mineral Petrol Sedimentol 1:2–32

Llambías EJ (1972) Estructura del Grupo Volcánico Farellón Negro, Catamarca, República Argentina. Rev Asoc Geol Argent 27:161–169

Longerich HP, Günther D, Jackson SE (1996) Elemental fractionation in laser ablation inductively coupled plasma-mass spectrometry. Fresenius J Anal Chem 355:538–542

Márquez-Zavalía MF (1988) Mineralogía y génesis del yacimiento Capillitas (Catamarca, República Argentina). Ph.D Thesis, Universidad Nacional de Salta. 284 pp

Márquez-Zavalía MF (1999) El yacimiento Capillitas, provincia de Catamarca In: Zappettini EO (ed) Recursos Minerales de la República Argentina. SEGEMAR, Anales 35, pp 1643–1652

Márquez-Zavalía MF (2006) El extremo rico en As de la serie Jordanita-Geocronita de Capillitas, Catamarca, Argentina. Rev Asoc Geol Argent 61:231–235

Márquez-Zavalía MF (2008) La rodocrosita de Mina Capillitas "Piedra" Nacional Argentina – Rosa del Inca. Sitios de Interés Geológico de la República Argentina. In: CSIGA (ed) Instituto de Geología y Recursos Minerales. Servicio Geológico Minero Argentino - SEGEMAR. Anales 46(I):85–98 (Spanish). Buenos Aires

Márquez-Zavalía MF, Craig JR (2004) Telluride and precious metal mineralization at Mina Capillitas, Northwestern Argentina. Neues Jb Mineral Monat 2004(4):176–192

Márquez-Zavalía MF, Galliski MA (2007) Chatkalita, nekrasovita y otros minerales del grupo de la estannita de veta María Eugenia, Cerro Atajo, Catamarca, Argentina. Rev Asoc Geol Argent 62:289–298

Marquez-Zavalía MF, Heinrich CA (2011) Porphyry-style to epithermal Cu-Au mineralization associated with the Farallón Negro Volcanic Complex, NW Argentina. SGA Conference Field Trip F5 Guide Book

Martinez F, Fogliata A, Montenegro N, Hagemann SG (2011) Geology, mineralogy and geochemistry of the Au-Mn Farallón Negro Rama Norte vein in the epithermal low-sulfidation Farallón Negro deposit, Argentina. 11th Bienn SGA Meet, pp 726–728

McBride SL (1972) A potassium-argon age investigation of igneous and metamorphic rocks from Catamarca and La Rioja provinces, Argentina. PhD Dissertation, Queen's University, Kingston, Canada

McQueen HWS, Beaumont C (1989) Mechanical models of tilted block basins. In: Price RA (ed) IUGG-AGU Geophys Monogr 48, pp 25–32

Meier DL (2008) Low-salinity fluids at the Bajo de la Alumbrera porphyry Cu-Au deposit, Argentina. MSc Thesis, ETH Zürich. 68 pp

Meier DL, Heinrich CA, Guillong M, Marquez-Zavalía MF (2008) Low-salinity fluids at the Bajo de la Alumbrera porphyry Cu-Au deposit, Argentina. Swiss Geoscience Meeting 2008. Lugano, Switzerland

Mendez V (1997) Yacimiento Bajo La Alumbrera, provincia de Catamarca, República Argentina. Rev Asoc Argent Geol Econ 11:15–30

Mon R (1976) La tectonica del borde oriental de los Andes en las provincias de Salta, Tucumán y Catarnarca, República Argentina. Rev Asoc Geol Argent 31:65–72

Montenegro N, Morales F (2004) Distrito mineralizado Farallón Negro. Yacimientos Mineros Agua de Dionisio, Belén, provincia de Catamarca, República Argentina. In: Márquez-Zavalía MF (ed) Curso Latinoamericano de Metalogenia UNESCO-SEG. Guía de campo, Mendoza, pp 83–99

Mugas-Lobos AC, Márquez-Zavalía MF, Galliski MA (2012) Minerales de mena del depósito epitermal de baja sulfuración Don Sixto, Mendoza. Rev Asoc Geol Argent 69:3–12

Müller D, Forrestal P (1998) The shoshonite porphyry Cu-Au association at Bajo de la Alumbrera, Catamarca province, Argentina. Mineral Petrol 64:47–64

Müller D, Forrestal P (2000) The shoshonite porphyry Cu-Au association at Bajo de la Alumbrera, Catamarca province, Argentina: a reply. Mineral Petrol 68:305–308

Navarro H (1986) Geología general y económica del pórfido de Cu-Mo "Mi Vida". Rev Inst Geol Min. Jujuy, Argentina 6: 127–154

Peacor DR, Dunn PJ, Ramik RA, Sturman BD, Zeihen LG (1985) Philipsburgite, a new copper zinc arsenate hydrate related to kipushite, from Montana. Can Mineral 23:255–258

Peirano A (1944) Agua de Dionisio. Un centro volcánico moderno en el distrito de Hualfín, departamento de Belén, provincia de Catamarca. Cuad Mineral Geol Tucumán 3:12

Pettke T, Halter WE, Webster JD, Aigner-Torres M, Heinrich CA (2004) Accurate quantification of melt inclusion chemistry by LA-ICPMS: a comparison with EMP and SIMS and advantages and possible limitations of these methods. Lithos 78:333–361

Pettke T, Oberli F, Audetat A, Guillong M, Simon AC, Hanley JJ, Klemm LM (2012) Recent developments in element concentration and isotope ratio analysis of individual fluid inclusions by laser ablation single and multiple collector ICP-MS. Ore Geol Rev 44:10–38

Pokrovski GS, Borisova AY, Harrichoury JC (2008) The effect of sulfur on vapor–liquid fractionation of metals in hydrothermal systems. Earth Planet Sci Lett 266(3–4):345–362

Pouchou JL, Pichoir F (1985) "PAP" (ϕρZ) correction procedure for improved quantitative microanalysis. In: Armstrong JT (ed) Microbeam analysis. San Francisco Press, San Francisco, pp 104–106

Proffett JM (2003) Geology of the Bajo de la Alumbrera porphyry copper-gold deposit, Argentina. Econ Geol 98:1535–1574

Putz H, Paar WH, Topa DA (2009) Contribution to the knowledge of the mineralization at mina Capillitas, Catamarca. Rev Asoc Geol Argent 64:514–524

Quartino BJ (1962) Sobre la interpretación geológica del distrito volcánico de Farellón Negro (Provincia de Catamarca). 1 Cong Geol Argentino 2:267–278

Ramos VA (1977) Basement tectonics from LANDSAT imagery in mining exploration. Geol Mijnbouw 56(3):243–252

Ramos VA (1999) In: Caminos R (ed) Las Provincias Geológicas del Territorio Argentino. Geología Argentina, Buenos Aires, pp 41–96

Rauchenstein-Martinek K, Wagner T, Wälle M, Heinrich CA (2014) Gold concentrations in metamorphic fluids: a LA-ICPMS study of fluid inclusions from the Alpine orogenic belt. Chem Geol 385:70–83

Reich M, Kesler SE, Utsunomiya S, Palenik CS, Chryssoulis SL, Ewing RC (2005) Solubility of gold in arsenian pyrite. Geochim Cosmochim Acta 69(11):2781–2796

Richards JP (2011) Magmatic to hydrothermal metal fluxes in convergent and collided margins. Ore Geol Rev 40:1–26

Richards JP (2013) Giant ore deposits formed by optimal alignments and combinations of geological processes. Nat Geosci 6:911–916

Richards JP, Bray CJ, Channer DMD, Spooner ETC (1997) Fluid chemistry and processes at the Porgera gold deposit, Papua New Guinea. Mineral Deposita 32:119–132

Roco R, Koukharsky M (1999) El pórfiro cupro-molibdenífero Agua Rica y las manifestaciones hidrotermales asociadas, Catamarca. In: Zapettini EO (ed) Recursos Minerales de la República Argentina, SEGEMAR, Anales 35, Buenos Aires, pp 1479–1492

Rojas N, Perelló J (2004) El yacimiento de Agua Rica, un depósito de cobre, molibdeno y oro, provincia de Catamarca, Argentina. In: Márquez-Zavalía MF (ed) Curso Latinoamericano de Metalogenia UNESCO-SEG. Guía de campo, Mendoza, pp 121–144

Rusk BG, Reed M, Dilles JH (2008) Fluid inclusion evidence for magmatic–hydrothermal fluid evolution in the porphyry copper–molybdenum deposit, Butte, Montana. Econ Geol 103:307–334

Salado Paz N, Fogliata AS, Avila JC, Montenegro N (2011) Veta Esperanza Sudeste, un caso particular de enriquecimiento Supergénico en el yacimiento Alto de la blenda, distrIto minero Agua de Dionisio, provincia de Catamarca. Rev Asoc Geol Argent 68:185–194

Sasso AM (1997) Geological evolution and metallogenetic relationships of the Farallón Negro Volcanic Complex, NW Argentina. Ph.D Dissertation, Queen's University, Kingston, Canada

Sasso AM, Clark AH (1998) The Farallón Negro group, northwest Argentina: magmatic, hydrothermal and tectonic evolution and implications for Cu-Au metallogeny in the Andean back-arc. SEG Newsl 34(1):8–18

Sasso AM, Clark AH (1999) El Grupo Farallón Negro: Evolución magmática, hidrotermal y tectónica e implicancias para la metalogenia de cobre-oro en el retroarco andino, Catamarca. In: Zapettini EO (ed) Recursos Minerales de la República Argentina, SEGEMAR, Anales 35, Buenos Aires, pp 1437–1450

Scott SD, Barnes HL (1971) Sphalerite geothermometry and geobarometry. Econ Geol 66:653–669

Seo JH, Heinrich CA (2013) Selective copper diffusion into quartz-hosted vapor inclusions: evidence from other host minerals, driving forces, and consequences for Cu-Au ore formation. Geochim Cosmochim Acta 113:60–69

Seo JH, Guillong M, Aerts M, Zajacz Z, Heinrich CA (2011) Microanalysis of S, Cl and Br in fluid inclusions by LA-ICP-MS. Chem Geol 284:35–44

Sillitoe RH (1973) The tops and bottoms of porphyry copper deposits. Econ Geol 68:799–815

Sillitoe RH (1976) Andean mineralization: a model for the metallogeny of convergent plate margins. Geol Assoc Can Spec Pap 14:59–100

Sillitoe RH (2010) Porphyry copper systems. Econ Geol 105:3–41

Sillitoe RH, Hedenquist J (2003) Linkages between volcanotectonic settings, ore-fluid compositions, and epithermal precious-metal deposits. Soc Econ Geol Spec Publ 10:315–343

Simmons SF, Brown KL (2006) Gold in magmatic hydrothermal solutions and the rapid formation of a giant ore deposit. Science 314(5797):288–291

Simmons SF, Brown KL (2007) The flux of gold and related metals through a volcanic arc, Taupo Volcanic Zone, New Zealand. Geology 35:1099–1102

Simpson MP, Palinkas SS, Mauk JL, Bodnar RJ (2015) Fluid inclusion chemistry of adularia-sericite epithermal Au-Ag deposits of the southern Hauraki Goldfield, New Zealand. Econ Geol 110:763–786

Sister RG (1963) Informe geológico-económico de Farallón Negro y zona adyacente, distrito Hualfín, dpto. Belén, provincia de Catamarca. Opera Lilloana 8:1–164

Sister RG (1965) Proyecto Minero Industrial Farallón Negro. Anexo I: Informe geológico. Informe YMAD (unpublished), Tucumán

Stefánsson A, Seward TM (2004) Gold(I) complexing in aqueous sulphide solutions to 500_C at 500 bar. Geochim Cosmochim Acta 68: 4121–4143

Suchomel BJ (1983) An economic geologic evaluation of the Bajo de Agua Tapada base and precious metal prospect, Catamarca province, Argentina. U. N. Dev Program, New York

Ulrich T, Heinrich CA (2002) Geology and alteration geochemistry of the porphyry Cu-Au deposit at Bajo de la Alumbrera, Argentina. Econ Geol 97:1865–1888

Ulrich T, Günther D, Heinrich CA (1999) Gold concentrations of magmatic brines and the metal budget of porphyry copper deposits. Nature 399:676–679

Ulrich T, Günther D, Heinrich CA (2002) The evolution of a porphyry Cu-Au deposit, based on LA-ICP-MS analysis of fluid inclusions: Bajo de la Alumbrera, Argentina. Econ Geol 97:1889–1920

Viramonte JG, Galliski MA, Araña Saavedra V, Aparicio A, García Cacho L, Martín Escorza C (1984) El finivulcanismo básico de la depresión de Arizaro, provincia de Salta. 9 Cong Geol Argentino 3:234–251

Von Quadt A, Erni M, Martinek K, Moll M, Peytcheva I, Heinrich CA (2011) Zircon crystallization and the lifetimes of ore-forming magmatic-hydrothermal systems. Geology 39:731–734

Wall V (1997) Bajo de la Alumbrera (Argentina). A world class copper-gold deposit. Rev Asoc Argent Geol Econ 11:92–93

Wallier S, Rey R, Kouzmanov K, Pettke T, Heinrich CA, Leary S, O'Connor G, Tamas CG, Vennemann T, Ullrich T (2006) Magmatic fluids in the breccia-hosted epithermal Au-Ag deposit of Roşia Montană, Romania. Econ Geol 101:923–954

Whitney DL, Evans BW (2010) Abbreviations for names of rock-forming minerals. Am Mineral 95:185–187

Wilkinson JJ (2013) Triggers for the formation of porphyry ore deposits in magmatic arcs. Nat Geosci 6:917–925